A three-dimensional statistical approach to improved image quality for multislice helical CT

Jean-Baptiste Thibault[a)]
Applied Science Laboratory, GE Healthcare, 3000 N. Grandview Boulevard, W-1180, Waukesha, Wisconsin 53188

Ken D. Sauer[b)]
Department of Electrical Engineering, 275 Fitzpatrick, University of Notre Dame, Notre Dame, Indiana 46556-5637

Charles A. Bouman[c)]
School of Electrical Engineering, Purdue University, West Lafayette, Indiana 47907-0501

Jiang Hsieh[d)]
Applied Science Laboratory, GE Healthcare, 3000 N. Grandview Boulevard, W-1180, Waukesha, Wisconsin 53188

(Received 12 December 2006; revised 28 August 2007; accepted for publication 30 August 2007; published 29 October 2007)

Multislice helical computed tomography scanning offers the advantages of faster acquisition and wide organ coverage for routine clinical diagnostic purposes. However, image reconstruction is faced with the challenges of three-dimensional cone-beam geometry, data completeness issues, and low dosage. Of all available reconstruction methods, statistical iterative reconstruction (IR) techniques appear particularly promising since they provide the flexibility of accurate physical noise modeling and geometric system description. In this paper, we present the application of Bayesian iterative algorithms to real 3D multislice helical data to demonstrate significant image quality improvement over conventional techniques. We also introduce a novel prior distribution designed to provide flexibility in its parameters to fine-tune image quality. Specifically, enhanced image resolution and lower noise have been achieved, concurrently with the reduction of helical cone-beam artifacts, as demonstrated by phantom studies. Clinical results also illustrate the capabilities of the algorithm on real patient data. Although computational load remains a significant challenge for practical development, superior image quality combined with advancements in computing technology make IR techniques a legitimate candidate for future clinical applications. © *2007 American Association of Physicists in Medicine*. [DOI: 10.1118/1.2789499]

Key words: computed tomography, iterative reconstruction, multislice helical, Bayesian estimation, maximum *a posteriori*, coordinate descent optimization

I. INTRODUCTION

Multislice CT scanning is particularly attractive for clinical applications due to short acquisition times, thin slices, and large organ coverage. Those acquisition trajectories produce projection measurements that pass obliquely through the 2D reconstructed image planes. As the pitch increases, deviation from conventional approximate two-dimensional planar data is further amplified. The accurate handling of this geometry is critical to the elimination of unwanted reconstruction artifacts and the enhancement of image quality. Recent developments in analytical inversion algorithms give reason to hope that for many, applications, image quality may be adequate under single-pass, deterministic inversion culminating in data backprojection.[1,2] Imaging applications arise, however, in which characteristics of the scanner hardware place a limit on the quality of reconstructions. Helical "windmill" artifacts may originate from portions of patient anatomy, particularly in the case of abrupt edges in high-contrast materials, such as bones and prosthetics.[3] Clinical diagnostics also require the resolution of detail beyond the capability of even recent scanners.

Traditionally, images have been reconstructed from CT data using so-called analytical reconstruction algorithms such as filtered backprojection (FBP) or convolution backprojection (CBP). Some algorithms completely neglect the cone-beam geometry of the measured data during backprojection, and rely instead on helical projection data interpolations to limit the extent of geometric artifacts.[4–7] Other algorithms consider the cone-beam geometry by calculating nutating image planes to minimize the error between the reconstruction plane and the projection ray paths in a 2D backprojection step. These include the pi-algorithms,[8,9] ASSR,[10] or AMPR.[11] However, these approaches are not sufficient when the cone angle gets larger, and it becomes necessary to consider the exact acquisition geometry in a 3D backprojection step, such as in the Feldkamp (FDK) algorithm,[12] which has been modified and generalized for general multislice CT.[13–15] All these approaches are approximate by nature and

reduce rather than eliminate cone-beam artifacts. By contrast, the algorithms of Katsevich[16] provide an analytic solution to the helical cone beam scan inversion, with the hope of completely eliminating cone-beam artifacts. However, they were originally derived under the assumption of continuously sampled detector surfaces, not the discrete form necessary with hardware realizable in the foreseeable future. Although modifications have been proposed for a detector with discrete sampling,[17] these still do not offer the possibility to easily incorporate scanner-specific characteristics in the system model. In addition, most single backprojection-based techniques depend on projection data interpolation schemes, which limit the resolution characteristics of the final output.

As an attempt to provide more flexibility in the reconstruction choices, iterative reconstruction (IR) algorithms have been recently introduced for multislice helical CT images.[18–21] Enabled by recent advances in computer processing hardware[22] or additional algorithm developments[23] necessary to handle the additional computational cost, IR methods are now considered an emerging reconstruction technique for clinical CT patient data, with the objective of improving image quality in situations challenging for state-of-the-art convolution backprojection. Modern medical CT imaging demands low-dose scans, high resolution reconstructions, and artifact reduction even when data are limited or incomplete. Fortunately, IR techniques are particularly well equipped to address these challenges, although at the cost of longer reconstruction time.

Successful methods adapted for iterative reconstruction from CT data are based on the statistics of random fluctuations in sinogram measurements.[24–26] Rather than manipulating data to force it to conform to traditional analytical reconstruction models, statistical methods attempt, to the degree possible, to explicitly include nonidealities in the problem description. This view of image reconstruction requires only knowledge of a description of the way in which each measurement is influenced by unknown image values. Such deficiencies in data as Poisson counting noise and incomplete scan coverage are expected and their description is built into the reconstruction process. Rather than treating all measurements with equal weighting, a statistical model allows different degrees of credibility among data. This modeling provides statistical methods a robustness not easily incorporated into single backprojection techniques. Problem formulation for image reconstruction becomes the expression of a statistical measure relating sinogram data to the estimated image volume, in the form of an objective function, which may be solved iteratively. The addition of a stabilizing function in the form of a regularization prior may further reduce artifacts and image noise. *A priori* information about the distribution of the image space, such as an image smoothness penalty, provides another tool for controlling image quality.

This view of the reconstruction problem represents a significant departure from conventional analytical techniques. The nonquadratic nature of the objective function often resulting from modeled image statistics affects the usual tradeoff between image noise and resolution. While the choice of appropriate filter kernels represents the principal method of adapting image characteristics to clinician's expectations for single backprojection-based techniques, several elements of statistical IR methods may be tuned simultaneously to maximize image quality. However, the texture of IR images, a consequence of statistical modeling, requires careful investigation of the practical facets of image quality (contrast, noise, resolution) to warrant application to clinical diagnostics.

Since the introduction of IR methods to CT, much of the effort has been devoted to demonstrating the feasibility of the proposed techniques and illustrating some of its benefits in the general case. The results in this paper focus on demonstrating the value of iterative reconstruction in reducing artifacts, improving resolution, and lowering noise in reconstructed images. The great majority of artifacts we attack, as well as limitations in reconstruction resolution, result from the combination of detector aperture width and limited sampling rates. Section II introduces the general framework of the statistical reconstruction problem, and shows the formulation of the objective function. Section III presents more details on the forward modeling calculations, leading to accurate reconstructions. A novel approach to regularization is introduced in Sec. IV, with the design of a general family of convex potential functions flexible enough to provide sufficient control over desired final image quality. An efficient technique for the iterative solution of the optimization problem is then reviewed in Sec. V. Finally, using the scans and techniques introduced in Sec. VI, the results presented in Sec. VII demonstrate both superior spatial resolution performance and helical artifact reduction over analytical methods, thus positioning IR methods for future clinical use.

II. STATISTICAL MODEL FOR IMAGE RECONSTRUCTION

Let $\mathbf{x}=\{x_j; j \in \{1,\ldots,M\}\}$ be the discrete vector of three-dimensional image space. Its elements represent attenuation coefficients, or unknown densities of the elements of space forming the 3D volume and are the object of the reconstruction. Let $y=\{y_i; i \in \{1,\ldots,N\}\}$ be the discrete vector of projection measurements, representing the line integrals through the imaged object for a variety of positions and projection angles. Our IR algorithm uses the same calibrated and preprocessed data as conventional FBP.

An underlying assumption fundamental to the statistical formulation of the reconstruction problem is that $\mathbf{x}$ and $\mathbf{y}$ are random vectors, according to a common probability density function determined by patient anatomy and x-ray physics. The CT transmission scan does not provide the y_i directly, but rather is formed of a collection of recorded detector measurements $\{\lambda_i; i \in \{1,\ldots,N\}\}$ that are related to the line integral projections by Beer's law of attenuation.[27] They represent the detected x-ray intensity after attenuation by the scanned object, and follow a Poisson distribution:

$$\lambda_i \sim \text{Poisson}\{I_i e^{-\bar{y}_i}\},$$

where I_i is the impinging x-ray photon intensity, and $\bar{\mathbf{y}}$ is the ideal noiseless projection integral computed from the true 3D

attenuation values $\mathbf{x}$. The reconstruction problem may be formulated in the Bayesian framework as the maximum *a posteriori* (MAP) estimate

$$\hat{\mathbf{x}} = \arg\max_{\mathbf{x}} P(\mathbf{x}|\mathbf{y}),$$

where $P(.)$ denotes the probability, which is equivalent to

$$\hat{\mathbf{x}} = \arg\max_{\mathbf{x}} \{\log P(\mathbf{y}|\mathbf{x}) + \log P(\mathbf{x})\}. \quad (1)$$

Frequently, a model of the form $\mathbf{y}=\mathbf{A}\mathbf{x}+\mathbf{n}$ is used, linearizing the relation between $\mathbf{x}$ and $\mathbf{y}$ with the matrix $\mathbf{A}$, an operator transforming the image space in a manner similar to the CT scanning system. The noise values in $\mathbf{n}$ represent random fluctuations of the measurement about its mean as a result of photon and electronic noise.

The first term on the right-hand side of Eq. (1) is the log-likelihood term. A good approximation to the log-likelihood for the x-ray transmission problem is based on a second-order Taylor series expansion, in terms of the unknown image, and of the log of the Poisson probability mass function for the measurement counts λ_i.[28] This yields the quadratic expression:

$$\log P(\mathbf{y}|\mathbf{x}) \approx -\frac{1}{2}\sum_i d_i(y_i - [\mathbf{A}\mathbf{x}]_i)^2 + f(\mathbf{y})$$

$$= -\frac{1}{2}(\mathbf{y}-\mathbf{A}\mathbf{x})^T\mathbf{D}(\mathbf{y}-\mathbf{A}\mathbf{x}) + f(\mathbf{y}), \quad (2)$$

where $\mathbf{D}$ is a diagonal matrix, and $f(\mathbf{y})$ is some function of the data. For transmission tomography, the coefficients d_i of $\mathbf{D}$ are proportional to detector counts λ_i, which are maximum likelihood estimates of the inverse of the variance of the projection measurements.[28,29]

$$d_i \propto \lambda_i = I_i e^{-y_i} \cong \frac{1}{\sigma^2_{y_i}}. \quad (3)$$

The elements d_i in the quadratic form of Eq. (2) reflect inherent variations in credibility of data. For example, if a particular measurement y_i is photon-starved by some highly attenuating object, a problem which may cause artifacts in conventional images, the model reduces the weighting associated with that measurement by reducing the corresponding d_i. The dependence of the weighting matrix on the data differentiates this model from Gaussian approximations. The quality of the quadratic approximation in Eq. (2) improves as the signal-to-noise ratio grows, and is quite accurate for Poisson counts in the range of clinical CT.[28] We have recently proposed a more accurate noise model based on a compound Poisson-Gaussian model of the measurement counts for inclusion of electronic noise in the statistical model in cases where photon starvation occurs,[30] but the simple model of Eq. (3) was used to generate all results in this paper.

Combining Eq. (2) with the MAP estimate of Eq. (1) yields

$$\hat{\mathbf{x}} = \arg\min_{\mathbf{x}} \left\{ \frac{1}{2}(\mathbf{y}-\mathbf{A}\mathbf{x})^T\mathbf{D}(\mathbf{y}-\mathbf{A}\mathbf{x}) + U(\mathbf{x}) \right\}, \quad (4)$$

where $U(\mathbf{x})$ is a scalar regularization term that is equal to $\log P(\mathbf{x})$ within an additive constant. The function $U(\mathbf{x})$ typically penalizes local differences between voxel elements, and in Sec. IV we introduce a novel choice of $U(\mathbf{x})$ which is appropriate for our problem.

Note that FBP typically applies some kind of low-pass filtering of the noisy projection data to reduce noise in the low-signal regions. Whereas this is a form of statistical modeling, it is inaccurate, at best, as it does not consider the true distribution of the noise in the measurements. IR offers the opportunity to better model the physics of data acquisition. In practice, the measurement counts λ_i are subject to a number of calibration preprocessing steps, including physical distortions such as scatter and beam hardening corrections, and other specific scanner corrections such as detector response and normalization. Although they could be included directly in the forward model and the noise model,[31] in this paper we use the fully precorrected y_i directly in the quadratic form of Eq. (4), and rely on the robustness of the quadratic approximation for the typical dose levels of clinical CT scans.[28]

III. COMPUTATION OF THE FORWARD MODEL

The crucial advantage of statistical reconstruction methods is that they allow any choice of the matrix $\mathbf{A}$. Any scanning geometry can be accurately modeled by proper computation of the entries in $\mathbf{A}$, regardless of the three-dimensional sampling pattern. The model can be designed to realistically represent the scanner, although this may come at the cost of great computational expense. Because it is necessary to include the nonplanar character of the measurements of the helical scan in the forward model, a fundamental component of our approach is to compute the coefficients in the three spatial dimensions. The details of the calculation of the elements of the forward model lie at the core of any efficient implementation of the iterative algorithm, and often drive computation time and reconstruction accuracy.

The majority of projection algorithms in the literature are optimized for the projection of the complete image volume into the sinogram space. This is primarily because iterative reconstruction methods such as conjugate gradient (CG)[32] or ordered subsets (OS)[33] require a full forward and/or backprojection for each iteration. Consequently, the computation and memory requirements of some forward and backprojection operators have been optimized for this situation. Siddon's method[34] is one of the fastest algorithms recognized to date to directly compute the ray path through voxel space, using a parametric description of the ray. It has been optimized and improved upon with accelerations such as in Ref. 35. Other fast techniques propose simple incremental computations among image voxels for a single projection view in order to maximize performance. For instance, the distance-

driven (DD) method[36] leads to fast implementation without degrading the frequency response for rectangular basis functions.

On the other hand, voxel-based iterative algorithms, such as Gauss-Seidel (GS)[37] or the algorithm of Sec. V, may be preferred to projection-based techniques due to their convergence speed. Previously, we have calculated the forward projection using a solid voxel model,[18,19] which is based on the computation of the intersection between the ray path and 3D voxels in the helical cone-beam geometry using the Liang-Barsky line-clipping algorithm.[38] While this model can be very accurate, it is computationally expensive because it requires the projections of many rays per voxel/detector pair to account for the finite size of the detector and voxel elements. As an alternative, the DD kernel of Ref. 36 has been shown to produce images free of artifacts related to the forward model, so we propose here an implementation tailored to coordinate descent optimization algorithms. We operate directly in the native geometry of the scanner in order to avoid any loss of accuracy which might affect resolution performance. The computation for a single voxel consists of three steps repeated for each projection view:

(1) For each view angle, project the voxel's center onto the detector array.
(2) Estimate the 2D footprint of the voxel onto the detector array by appropriately magnifying a "flattened" version of the voxel and placing it at the position computed in (1). Notice that this footprint may overlap several detector elements.
(3) Apply the DD projection kernel per Eqs. (11) and (12) to compute the coefficients of the forward model for each element of the detector array within this neighborhood.

Figure 1 illustrates the spatially varying nature of the model in the native cone-beam geometry with a curved detector for two different positions of the source. The DD kernel can be considered as the convolution between the voxel response and the detector response. Let θ be the ray angle in the (x,y) plane parallel to the detector channel axis, and φ the angle in the (y,z) plane parallel to the detector row axis (see Fig. 2). Intuitively, our objective is to "flatten" the voxel along the dimension most closely parallel to the detector face. By flattening the voxel, we simplify the computation of its projection. Define the angle $\tilde{\theta}$ which results from selecting the 45° rotation of θ such that $|\tilde{\theta}| < \pi/4$:

$$\tilde{\theta} = \left(\theta + \frac{\pi}{4}\right) \bmod \frac{\pi}{4} - \frac{\pi}{4}. \tag{5}$$

Figure 2 shows how $\tilde{\theta}$ measures the angle between a ray passing through the voxel center, and a normal to the flattened voxel surface. We use a separable expansion of the 2D projection in the 3D case. The projection coefficient of **A** for voxel i, view j, channel k, row l, is therefore:

$$C_{i,j,k,l} = A_{i,j,k} \times B_{i,j,k,l}, \tag{6}$$

where, for rectangular basis functions in the cone-beam geometry, as illustrated in Fig. 2,

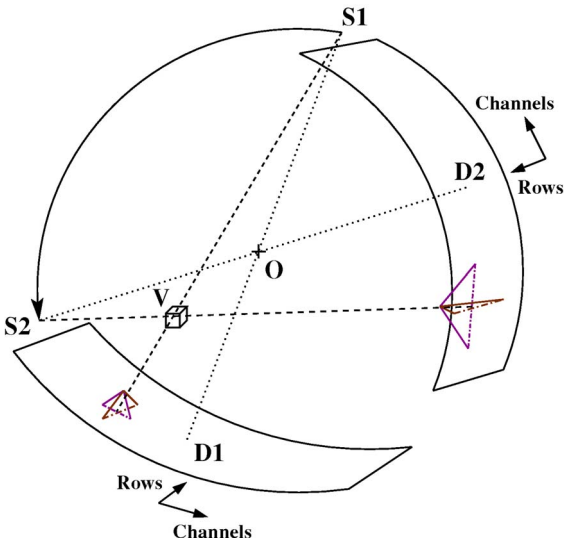

FIG. 1. Forward projection of a voxel V in 3D space using the native cone-beam geometry of the detector. A separable kernel between the channel and row directions is used to compute the coefficients. The resulting forward model is spatially varying, as illustrated by the size of the kernel which changes between source positions S_1 and S_2 as a function of the distance between voxel and detector.

$$A_{i,j,k} = \frac{\Delta_{xy}}{\cos\tilde{\theta}} V_c(\delta_c) * S_c(\delta_c), \tag{7}$$

$$B_{i,j,k,l} = \frac{1}{\cos\varphi} V_r(\delta_r) * S_r(\delta_r), \tag{8}$$

where Δ is the voxel size, δ is the distance between the center of the projected voxel and the center of the detector,

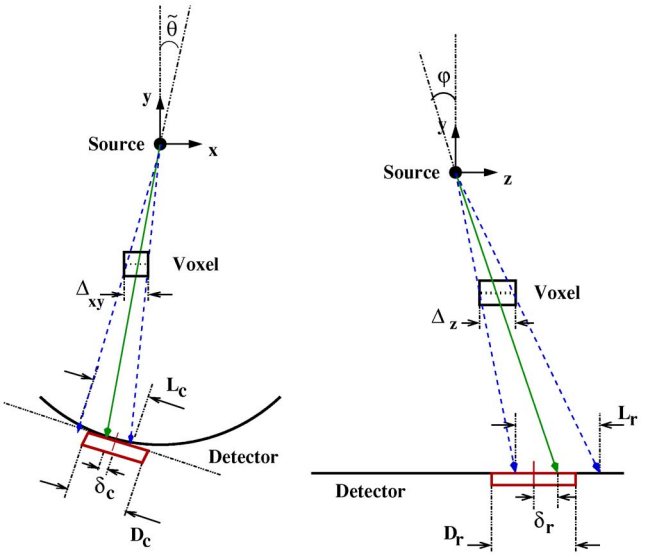

FIG. 2. Forward model computation by kernel-based magnification in multislice native cone-beam geometry. The model computes the projection of rectangular basis functions onto the detector along the detector channel dimension (left) and detector row dimension (right). A convolution model between voxel response and detector response is used to compute the coefficients.

$V(\cdot)$ is the voxel window, $S(\cdot)$ is the detector sensitivity function, and "*" denotes convolution. We use the subscripts c and r to denote the channel and the row dimensions of the multislice detector, respectively. With L as the length of the voxel projection onto the detector by magnification, and D as the size of the detector element, the DD kernel is

$$V(\delta) = \mathrm{rect}(\delta/L), \tag{9}$$

$$S(\delta) = \frac{1}{D}\mathrm{rect}(\delta/L). \tag{10}$$

Note that the inclusion of both the detector and the voxel response is important for reconstructions with high spatial sampling where is $L<D$ is possible. The coefficients of Eq. (6) are therefore

$$A_{i,j,k} = \frac{\Delta_{xy}}{\cos\tilde{\theta}}\mathrm{clip}\left[0, \frac{D_c + L_c}{2} - |\delta_c|, \min(L_c, D_c)\right], \tag{11}$$

$$B_{i,j,k,l} = \frac{1}{\cos\varphi}\mathrm{clip}\left[0, \frac{D_r + L_r}{2} - |\delta_r|, \min(L_r, D_r)\right]. \tag{12}$$

The function clip[ ] is $\mathrm{clip}[a,b,c]=\min(\max(a,b),c)$. This model also offers the possibility of easily including scanner-specific characteristics such as focal spot size and detector response nonuniformity, although, for the time-being, these effects are not taken into account.

IV. STABILIZING THE OBJECTIVE

Without the regularization term $U(\mathbf{x})$ in Eq. (4), it is well known that the image estimates are excessively noisy and unstable.[39,40] Regularization enforces smoothness in the reconstructed images by encouraging neighboring pixels to have similar values, and the parameters of the regularizing term are used to control the trade-off between noise and resolution in the final reconstruction.

In accordance with Eq. (1), we choose $U(\mathbf{x})$ as the negative log probability of a prior distribution. Typical choices for the prior distribution are Markov random fields (MRFs) because they result in a function $U(\mathbf{x})$ with only local interaction terms. A commonly used general class of MRFs takes the form of

$$U(\mathbf{x}) = \frac{1}{f(\sigma)}\sum_{\{j,k\}\in C}\Psi_\sigma(x_j - x_k), \tag{13}$$

where $\Psi(\cdot)$ is the potential function, penalizing local differences, and $f(\cdot)$ is some monotone increasing function. The parameter σ is a scalar that is determined empirically and controls the prior strength relative to the noise model over the local neighborhood defined by the set C of all 26 pairs of neighboring voxels in 3D. It is advantageous to regularize over a 3D neighborhood for reconstruction from cone-beam measurements.

The generalized Gaussian Markov random field (GGMRF)[41] is a class of MRFs with desirable properties which result in a regularization term of the form

$$U(\mathbf{x}) = \frac{1}{p\sigma^p}\sum_{\{j,k\}\in C} b_{j,k}\,\rho(x_j - x_k), \tag{14}$$

$$\rho(\Delta) = |\Delta|^p \quad p \geqslant 1. \tag{15}$$

The $b_{j,k}$ are directional weighting coefficients, which we choose as the inverse of the distance between the center voxel and the elements in C, normalized such that $\Sigma_{\{j,k\}\in C}\, b_{j,k}=1$. The exponent parameter p of the GGMRF in Eq. (15) allows one to control the degree of edge preservation in the reconstruction. As long as $p>1$, the resulting regularization term is strictly convex. Combined with Eq. (4), the resulting objective function is strictly convex as well, which guarantees a unique global minimum of the cost function and allows simpler optimization algorithms for the derivation of the solution. Convexity is desirable since it ensures that the reconstruction does not change discontinuously with the sinogram data.[41] When $p=2$, the regularization term is quadratic, and the reconstructed image tends to have softer edges. As p is reduced, the regularization term becomes nonquadratic and edge sharpness tends to be enhanced. Other choices of potential functions offer alternatives for varying edge sensitivity.[39,42–48] In general, regularization affects noise and resolution, and may preserve high and low contrast detail differently. Such flexibility is important to clinical imaging.

We next introduce a novel prior formulation, designed to provide flexibility over the GGMRF. It is a family of convex functions, which encompasses GGMRF and Huber-like functions.[45] This new potential function takes the form

$$\rho(\Delta) = \frac{|\Delta|^p}{1 + |\Delta/c|^{p-q}}. \tag{16}$$

The corresponding derivative is known as the influence function

$$\rho'(\Delta) = \frac{|\Delta|^{p-1}}{1 + |\Delta/c|^{p-q}}\left(p - \left(\frac{p-q}{c^{p-q}}\right)\frac{|\Delta|^{p-q}}{1 + |\Delta/c|^{p-q}}\right)\mathrm{sign}(\Delta). \tag{17}$$

We assume that $p \geqslant q \geqslant 1$. The constants p and q determine the powers near, and distant from the origin, respectively. The constant c determines the approximate threshold of transition between low and high contrast regions. We restrict ourselves to convex functions, that is $1 \leqslant q \leqslant p \leqslant 2$. The details of the convexity analysis can be found in the Appendix. We refer to this family of convex priors as the q-generalized Gaussian MRF (q-GGMRF). It contains interesting special cases for some values of p and q

- $p=1=2$: Gaussian prior
- $p=2$; $q=1$: Approximate Huber prior
- $1<q=p\leqslant 2$: Generalized Gaussian MRF
- $1\leqslant q<p\leqslant 2$: q-generalized Gaussian MRF

Figure 3 compares the influence function of the Gaussian and edge-preserving GGMRF priors to several q-GGMRF priors. In the Gaussian case, the influence function is linear

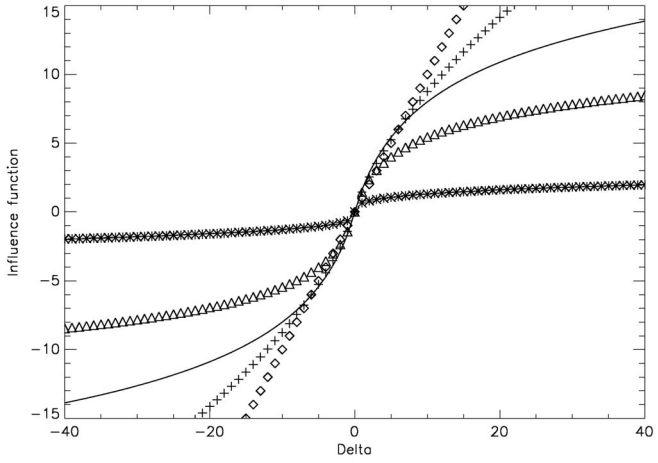

FIG. 3. Influence function for the q-GGMRF prior, plotted for different parameters p, q, and c, and across a range of local voxel differences. Δ relevant in a range of Hounsfield units relevant to clinical imaging. Solid line: q-GGMRF $p=2$, $q=1.2$, $c=10$. Asterisks: GGMRF $p=1.3$, $q=1.3$; open diamonds: Gaussian $p=2$, $q=2$. Open triangles: q-GGMRF $p=2$, $q=1.2$, $c=5$. Crosses: q-GGMRF $p=2$, $q=1.5$, $c=10$.

around the origin, the region which controls textures in uniform regions. With p fixed, smaller values of q retain better edge-preserving characteristics, as the influence becomes constant for larger values of Δ. The value of c controls the inflexion point: higher c pushes the edge-preserving behavior toward larger Δ. We will examine suitable values of the parameters p, q, and c for CT imaging in Sec. VII.

V. COMPUTATION OF THE SOLUTION

With the choice of a strictly convex prior potential function, the cost function defined in Eq. (4) is strictly convex as well, and therefore has a unique global minimum. For this reason, any number of different optimization algorithms will converge to the same reconstructed image corresponding to the global minimum of Eq. (4).[49] Therefore, the choice of optimization algorithm should be based on the computational efficiency by which the algorithm reaches the unique solution.

Statistical methods have a great advantage in the multislice helical case, in having little dependence in their implementation on the geometry of data collection. We attack the estimation/optimization of Eq. (4) in the same manner regardless of the scan pattern represented by $\mathbf{A}$ or the selected prior $U(\mathbf{x})$. We select an algorithm in the class of voxel-based techniques for their ability to quickly converge high-frequency components, provided a good initial condition, as can be quickly obtained with FBP. We propose optimization over the full 3D volume through a sequence of one-dimensional updates where the image estimate $\hat{\mathbf{x}}$ is

$$\hat{\mathbf{x}} = \arg\min_{\mathbf{x}\in\Omega}\left\{\frac{1}{2}(\mathbf{y}-\mathbf{A}\mathbf{x})^T\mathbf{D}(\mathbf{y}-\mathbf{A}\mathbf{x}) + \frac{1}{f(\sigma)}\sum_{\{j,k\}\in C} V_\sigma(x_j - x_k)\right\}, \tag{18}$$

and Ω is the convex set of non-negative reconstructions. The optimization of a strictly convex functional over a convex set yields a unique solution so the addition of this positivity constraint is valid. For image regularization, we use in practice the q-GGMRF of Sec. IV, but to emphasize that this method is independent of the particular choice of the prior for implementation, we employ the general form of Eq. (13) in Eq. (18). For implementation, our approach to the solution is a sequence of one-dimensional optimization steps, where all other image elements are fixed during a single element's update. Each one-dimensional optimization computes element x_j at iteration $(n+1)$ from $\mathbf{x}$ at iteration (n) based on

$$\hat{x}_j^{n+1} = \arg\min_{x_j\geqslant 0}\left\{\sum_{i=1}^{N}\frac{d_i}{2}(y_i - \mathbf{A}_{i*}\mathbf{x}^{(n)} + \mathbf{A}_{ij}(x_j^{(n)} - x_j))^2 + \frac{1}{f(\sigma)}\sum_{k\in C_j} V_\sigma(x_j - x_k^{(n)})\right\}. \tag{19}$$

We perform single voxel updates in random order to minimize the correlation between adjacent updates and maximize convergence speed.[50] At each step, the one-dimensional cost function in Eq. (19) must be minimized by computing the root of its derivative

$$\theta_1 + \theta_2(x - x_j^{(n)}) - \frac{1}{f(\sigma)}\sum_{k\in C_j} I_\sigma(x - x_k^{(n)})\Big|_{x=x_j^{(n+1)}} = 0, \tag{20}$$

where the first and second derivatives for the left-hand side of Eq. (19) yield

$$\theta_1 = \sum_{i=1}^{N} d_i A_{ij}(y_i - \mathbf{A}_{i*}\mathbf{x}^{(n)}), \tag{21}$$

$$\theta_2 = \sum_{i=1}^{N} d_i A_{ij}^2. \tag{22}$$

$I_\sigma(\cdot)$ is the influence function, i.e., the first derivative of the prior potential, and its expression for the q-GGMRF is given in Eq. (17). Because in general the nonquadratic shape of the regularizer does not lead to a closed-form solution, a simple half-interval search is performed, to some tolerance around the root.[29] The general framework of this iterative solution can be summarized as:

(1) Initialize $\mathbf{x}^{(0)}$ from FBP images
(2) Perform initial forward projection to compute $\mathbf{A}\mathbf{x}^{(0)}$
(3) Perform single image-space iteration
  (a) Select voxel $x_j^{(n)}$ according to random schedule
  (b) Calculate the elements of the forward model $\mathbf{A}_{*j}$
  (c) Compute θ_1 and θ_2

(d) Perform half-interval search to find the root of Eq. (20)
(e) Update $x_j^{(n+1)}$
(f) Update forward projection estimate $\mathbf{Ax}^{(n+1)}=\mathbf{Ax}^{(n)}+\mathbf{A}_{*j}(x_j^{(n+1)}-x_j^{(n)})$
(g) Repeat steps 3(a)–3(f) until all voxels have been visited

(4) Repeat full iteration until convergence is achieved $\forall j\in\{1\ldots M\}|x_f^{n+1}-x_j^{(n)}|<1$ HU

This approach, called iterative coordinate descent (ICD),[29] guarantees global and monotonic convergence for convex *a posteriori* log probability density functions,[51] and has shown rapid convergence properties provided a good choice of initial conditions. We use the standard FBP images as initial conditions, offering a good estimate of the low frequency components. While the cost of each iteration remains relatively high as compared to FBP, a full 3D ICD reconstruction typically converges in fewer than 10 iterations, to the point where successive image differences are smaller than the visible range of 1 HU.

We refer to the ICD approach to solving the MAP estimation problem posed in Eq. (4) as "MAP-ICD" in the remainder of this paper, to emphasize that the global solution to the reconstruction problem is in fact the combination of the choice of a cost function and the choice of an optimization algorithm, both of which may be made independently, within the limits of the ability of the optimization technique to handle the constraints of the statistical model.

VI. MATERIALS AND METHODS

We acquire data on the GE Lightspeed 16-slice third generation CT scanner to assess the performance of the algorithm. The Lightspeed geometry corresponds to 541.0 mm source-to-isocenter distance, and 949.075 mm source-to-detector distance. The elements of the multislice detector are formed on an arc concentric to the focal spot of the x-ray source. All the scans used here contain 984 views per rotation for a 1.0 s gantry period. In the following, we refer to scan sets by describing the detector configuration and scanning trajectories. The $R\times W$ notation represents a multislice scan taken with R detector rows, and where each row thickness is W mm at the isocenter of the CT gantry. Total detector aperture corresponds to the product $R\times W$ in millimeters. The helical pitch of acquisition is described as $P/R:1$, that is the number of detector rows P traveled along the axis of the gantry during one full rotation. The quantity P/R is often referred to as the normalized pitch of helical acquisition. In all images, the notation "WW" defines the window width in Hounsfield units (HU) selected to display the images.

First, we assess the performance of the q-GGMRF prior model and general image quality of the MAP-ICD algorithm. For this purpose, we use the GE Performance Phantom (GEPP).[27] It is formed of a Plexiglas™ insert with resolution bars and tungsten wires in water, and supports quantitative measurements of noise and resolution. The phantom was scanned in 16×0.625 mm helical mode at pitch 15/16:1, and 100 mA. Our objective is to select a set of parameters p, q, and c based on visual inspections of reconstructed images with parameters varied systematically across the range of convex prior behavior. We limit ourselves to convex priors in this discussion so as to preserve the global convergence properties of the algorithm. Our purpose is not to provide an extensive comparison to prior art, but rather to show that this prior is designed to perform well in the context of regularized iterative reconstruction of clinical CT images. To obtain comparable results for various shapes of the potential function, we match noise between the resulting images within a fixed ROI to less than 1 HU. Matching noise ensures that the strength of the prior relative to the noise model is similar in all images. While keeping two of the parameters p, q, and c fixed, we vary the other to study the impact on image quality.

With a proper choice of the prior model, our major concern is then the comparison of the MAP-ICD algorithm against conventional analytical reconstruction relative to these image quality characteristics: in-plane resolution / noise trade-off, cross-plane resolution, and helical artifacts. For comparison, we will consider "FBP," the 2D filtered backprojection with adaptive view-weighting[6,27] used as baseline; "FDK," a Feldkamp-based algorithm providing explicit modeling of the 3D cone-beam geometry during backprojection,[2] "conjugate FDK," a Feldkamp-based algorithm making use of conjugate samples during 3D backprojection to achieve better slice-sensitivity profile,[52] and "Katsevich," Katsevich's exact analytic inversion algorithm for 3D reconstruction.[16]

In the following experiments aimed at demonstrating resolution performance, and later the presence or absence of helical artifacts, we will use an anthropomorphic head phantom. While all algorithms treat the cone-beam geometry with different degrees of accuracy, the limited sampling of the fine details in the bone structure due to discrete scanner characteristics also generates artifacts, generally described as "windmill" artifacts.[3] The cracks in the skull that vary rapidly from plane to plane in our head phantom are a particularly strong source of artifacts, and also provide some visual insights into in-plane and cross-plane resolution, with realistic imaging for CT diagnosis.

An important goal of this study of iterative reconstruction is understanding its effect on cross-plane resolution in CT systems. In conventional linear, spatially invariant analysis, samples are placed in a uniform pattern, yielding a band of recoverable frequencies having an easily discernible shape and size. In contrast, complete analysis of potential helical CT resolution is necessarily a three-dimensional problem without such simple sampling patterns. To our knowledge, no such analysis has been published. However, it is known that displacement of samples from a rectangular pattern in other applications can improve the recovered bandwidth; one common example is interlaced television scanning.[53]

In helical scan CT, each view of data corresponds to a complete set of measurements for each channel and row location in the detector array, with incremental displacements of the patient between successive views even with high pitch. Consequently, the minimum sample spacing along the

z direction is typically much smaller than the size of the detector row elements. This high sampling rate in z means that, if the data include only extremely low-frequency in-plane information, the Nyquist criteria may be satisfied even for very high spatial cross-plane resolution. In practice, frequency content will be more uniform in the three variables, and therefore less dramatic improvement will be possible than is indicated by minimum z-spacing. While the maximum sampling rate in z is high, the cross-plane resolution is also limited by detector aperture and focal spot size.[27] However, oversampling has been used to recover resolution from spatially filtered data in other applications,[54] so it is reasonable to believe that it can be used in our problem to improve over classical reconstruction resolution as well.

For simplicity, we will assume that the x-ray source is a point, and that the object is imaged about the isocenter. We denote the effective detector aperture at the isocenter by W. This is the physical spacing of the detector rows multiplied by the ratio (source-to-iso)/(source-to-detector). The z measurements for the object are then approximately convolved with the function $h(z)=(1/W)\mathrm{rect}(z/W)$, where $h(z)$ is a square pulse centered at $z=0$ with width 1 and area 1. The frequency response in z is then given by the continuous time Fourier transform of $h(z)$, which is $\mathrm{sinc}(f/f_c)$, where $f_c=1/W$. The first null of the sinc function is then at $f=f_c$. For frequencies below this first null given by $f<f_c$, it is possible, in principle, to recover the desired resolution because the sinc function magnitude is greater than zero. For example, for a detector aperture size at iso of $W=1.25$ mm, the first null falls at $f_c=8$ lp/cm, so we might expect to be able to recover resolutions up to 8 lp/cm. Alternatively, for $W=0.625$ mm, the first null falls at $f_c=16$ lp/cm, so we might expect to be able to recover resolutions up to 16 lp/cm. However, direct reconstruction methods such as FBP typically fall far short of this resolution, as we will illustrate in Sec. VII. Iterative reconstruction, which explicitly models the extents of the detector cells and image voxels, has the potential to improve on this.

In order to illustrate this potential benefit, we will compute the frequency response of the reconstruction algorithm using an empirical method. Using the head phantom scan mentioned earlier, we will add to the sinogram the forward projection of five synthetic points within a 10 cm diameter from the isocenter in the center plane of the volume: one point at the isocenter, and two others on the vertical and the horizontal axis, respectively. The forward projection of these synthetic points is computed using the DD kernel of Sec. III. Adding the synthetic data to the original sinogram will allow consideration of the real scan statistics in the experiment. We will then reconstruct those impulses within the head data with both MAP-ICD and FBP. For this experiment only, we will use a Gaussian prior ($p=q=2$). We use these parameters so that the MAP reconstruction is linearly related to the data, and our results are therefore independent of the contrast level of the synthetic points. Varying the scale parameter, σ, of the *a priori* image model will produce varying resolution, with smaller σ yielding smoother response and less spatial resolution. After taking the difference between the reconstructions with and without the added impulses for both MAP-ICD and FBP, and averaging the reconstructed point spread functions across the five locations, we then sample the response in the frequency domain to form comparison plots.

For a more complete analysis, we will also provide further visual and quantitative evidence of superior cross-plane resolution performance with MAP-ICD. We will compare the reconstructions of the head phantom scanned in 16×1.25 mm at helical pitch 9/16:1 to 16×0.625 mm at both helical pitch 15/16:1 and 9/16:1, where higher sampling resulting from $W=0.625$ mm will yield results closer to ground truth, with pitch 15/16:1 approaching the original scan trajectory of 16×1.25 mm at 9/16:1, and pitch 9/16:1 providing even finer sampling. For another quantitative measure, we will use a wire-in-air phantom, containing six wires inside a 20 cm circular phantom, with each wire sloped with a ratio of 4:1 relative to the z axis. Using partial volume effect in the reconstructed axial images, the profile through the wires will be computed and averaged over all wire locations to yield the measured slice sensitivity profile (SSP), comparing MAP-ICD to FBP for all three scan trajectories considered earlier. Finally, for a more systematic visual evaluation of cross-plane resolution, a suitable grid pattern aligned perpendicular to the z axis will be used. We will provide reconstructions of the high-resolution insert of the AAPM CT performance phantom (described in a report by the AAPM Task Force on CT Scanner Phantoms, approved by the American Association of Physicists in Medicine[55]), which is generally accepted as a challenging case in visual resolution studies. It features low-contrast holes ranging from 0.4 to 1.1 mm at intervals of 0.1 mm. We will repeat scans for all protocols considered above after placing the AAPM phantom upright on the CT table, and perform reconstructions followed by multiplanar reformats.

While improved cross-plane resolution performance with MAP-ICD is one of the major results we present in this paper, it is also important to confirm that helical "windmill" artifacts are controlled as well. To further emphasize the effect of limited sampling, we scan the head phantom with a wide detector pitch, using 16×1.25 mm at helical pitch 15/16:1. We will compare the results of MAP-ICD with each of FBP, FDK, Conjugate FDK and Katsevich to study robustness against helical artifacts. We will also consider a helical rib phantom scanned in 8×1.25 mm and helical pitch 13.4/8:1. The Teflon ribs oriented to change very rapidly from plane to plane, as well as the tapered hole in the center of the phantom, typically increase the level of helical artifacts, especially at high helical pitch.

Before getting to the results, we define the filter kernels used in the FBP images as "standard" or "bone" with the following characteristics demonstrated on the 0.05 mm tungsten wire submerged in water of the GEPP and scanned axially at 120 kV, 200 mA, and reconstructed at 5 mm thickness. Resolution is measured in line pairs per centimeter (lp/cm). The bone kernel is a high-frequency emphasis filter, designed as explained in Ref. 27, with a 50% MTF of 8.6 lp/cm and 10% MTF of 11.9 lp/cm for a corresponding

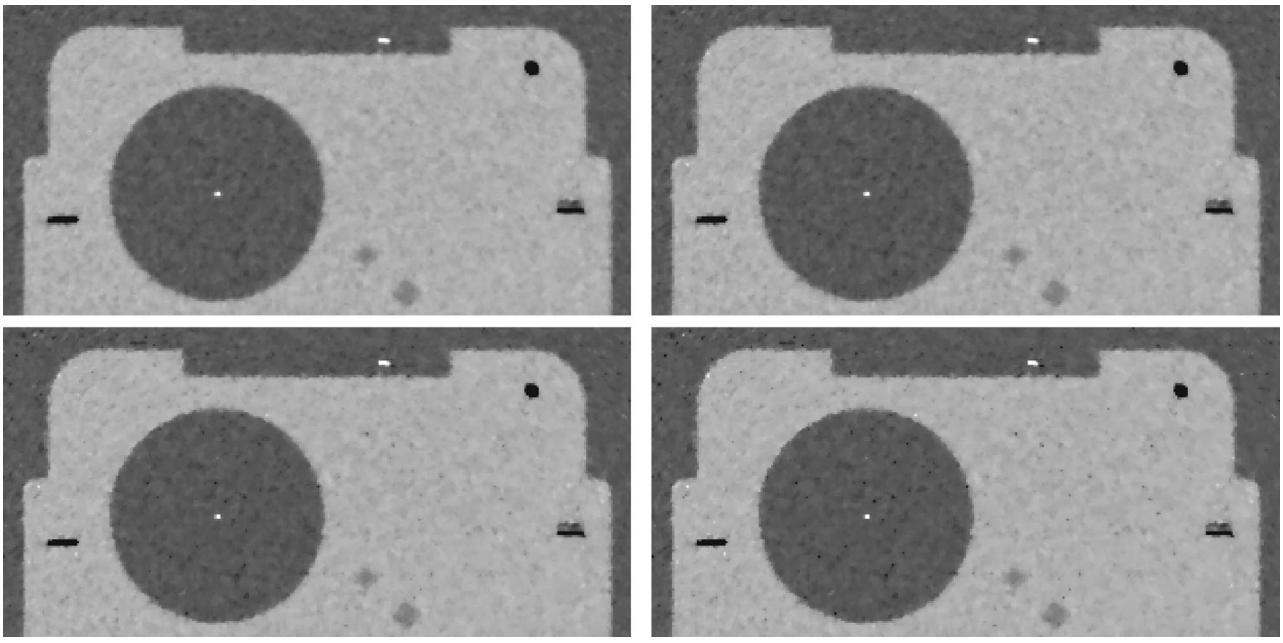

FIG. 4. Influence of the exponent parameter p of the q-GGMRF on image quality at matched noise with MAP-ICD on a GE Performance Phantom: 16 $\times$0.0625 mm, helical pitch 15/16:1, 100 mA, 1 s/rotation, WW=350; $\Delta x=\Delta y=0.488$ mm, $\Delta z=0.625$ mm; Top left panel: q-GGMRF $p=2.0$, $q=1.2$, $c=10$. Top right panel: q-GGMRF $p=1.6$, $q=1.2$, $c=10$. Bottom left panel: GGMRF $p=1.2$, $q=1.2$, $c=10$. Bottom right panel: GGMRF $p=1.1$, $q=1.1$, $c=10$. For q and c fixed panel, smaller p favors plateauing and salt-and-pepper noise in homogeneous regions.

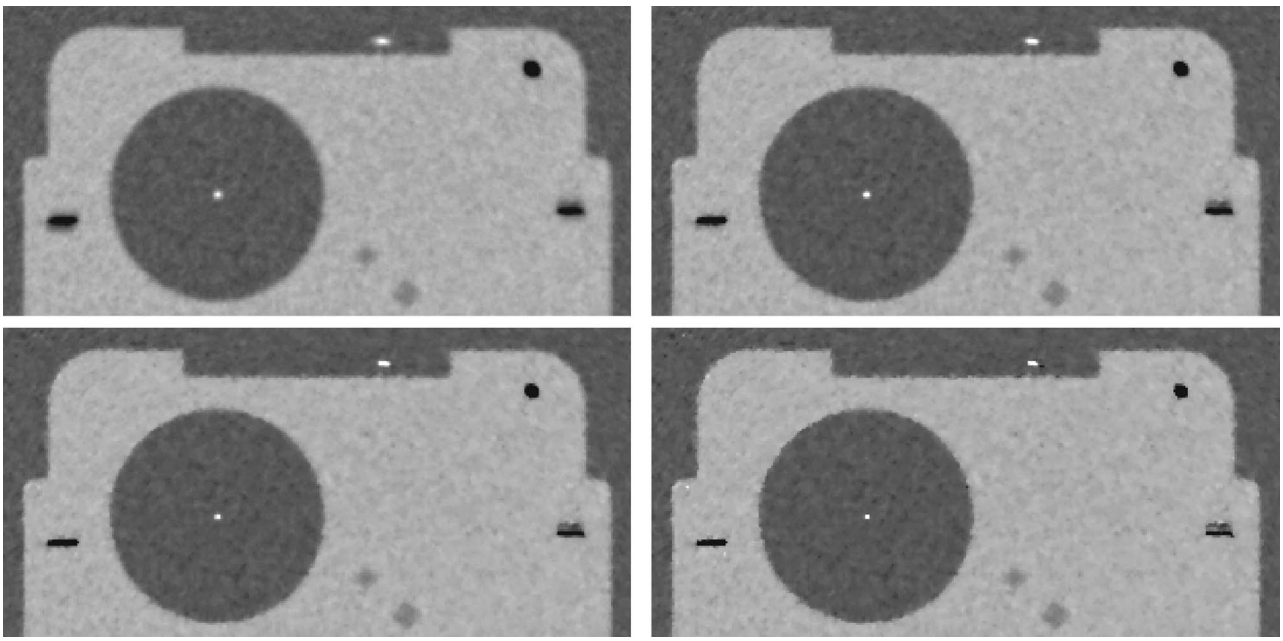

FIG. 5. Influence of the exponent parameter q of the q-GGMRF on image quality at matched noise with MAP-ICD on a GE Performance Phantom: 16 $\times$0.625 mm, helical pitch 15/16:1, 100 mA, 1 s/rotation, WW=350; $\Delta x=\Delta y=0.488$ mm, $\Delta z=0.625$ mm. Top left panel: Gaussian $p=2.0$, $q=2.0$, $c=10$. Top right panel: q-GGMRF $p=2.0$, $q=1.4$, $c=10$. Bottom left panel: q-GGMRF $p=2.0$, $q=1.2$, $c=10$. Bottom right panel: q-GGMRF $p=2.0$, $q=1.0$, $c=10$. For $p=2.0$ and $c=10$ fixed, smaller q leads to higher resolution.

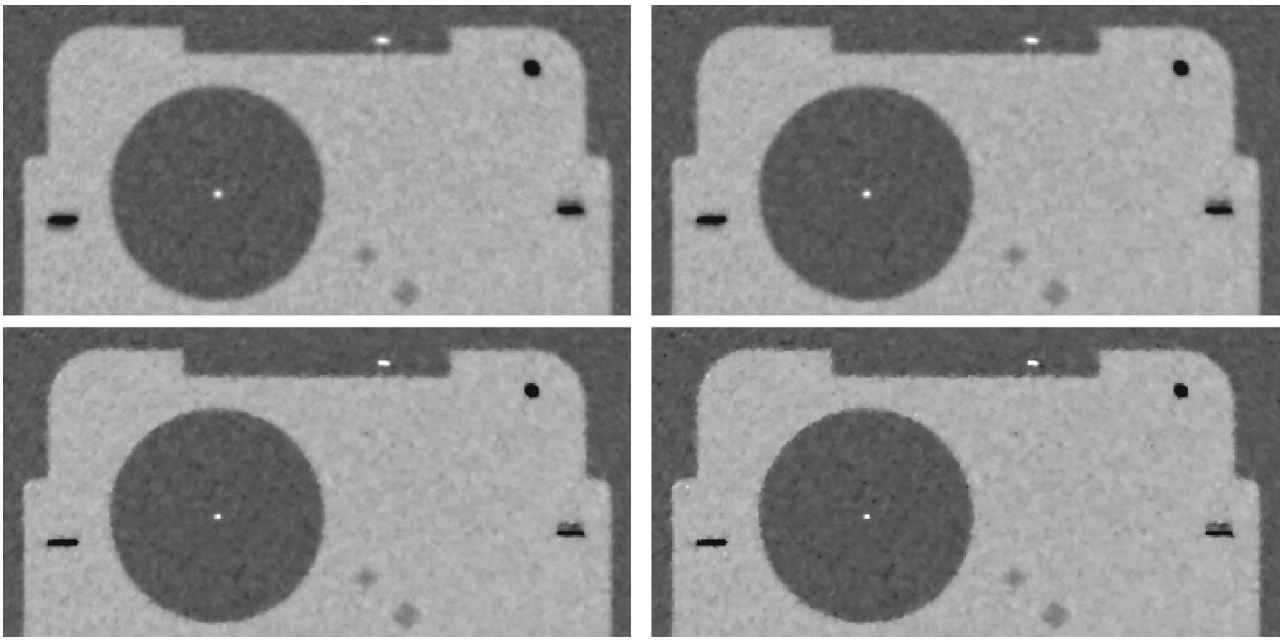

FIG. 6. Influence of the threshold parameter c of the q-GGMRF on image quality at matched noise with MAP-ICD on a GE Performance Phantom: 16×0.625 mm, helical pitch 15/16:1, 100 mA, 1 s/rotation, WW=350; $\Delta x = \Delta y = 0.488$ mm, $\Delta z = 0.625$ mm. Top left panel: q-GGMRF $p=2.0$, $q=1.2$, $c=1000$. Top right panel: q-GGMRF $p=2.0$, $q=1.2$, $c=100$. Bottom left panel: q-GGMRF $p=2.0$, $q=1.2$, $c=10$. Bottom right panel: q-GGMRF $p=2.0$, $q=1.2$, $c=1$. For p and q fixed, large values of c result in excessive smoothing.

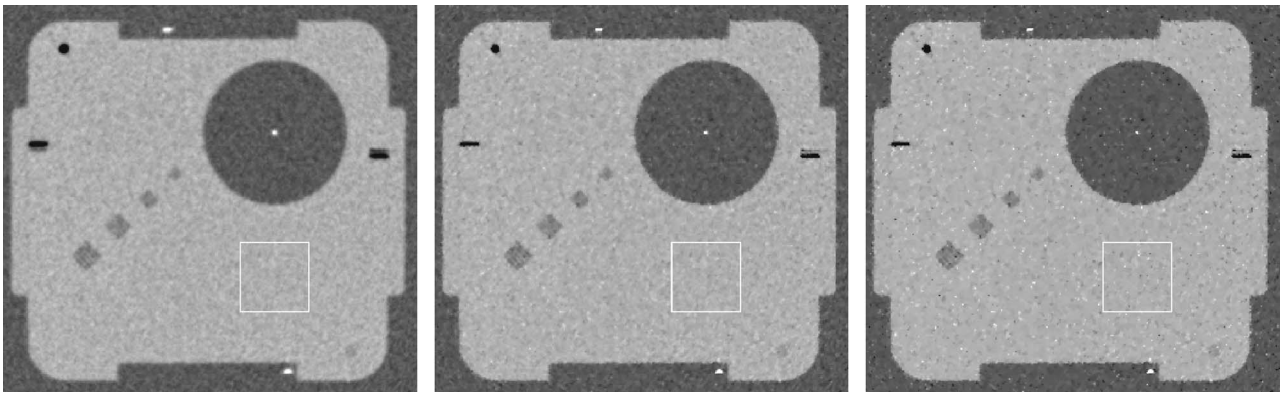

FIG. 7. Assessment of q-GGMRF image quality with MAP-ICD on a GE Performance Phantom: 16×0.625 mm, helical pitch 15/16:1, 100 mA, 1 s/rotation, WW=350; $\Delta x = \Delta y = 0.488$ mm, $\Delta z = 0.625$ mm. Left panel: Gaussian prior $p=2.0$, $q=2.0$, $\sigma=10$. Center panel: q-GGMRF prior $p=2.0$, $q=1.2$, $c=10$, $\sigma=8$. Right panel: GGMRF prior $p=1.1$, $q=1.1$, $\sigma=0.1$.

TABLE I. Noise and in-plane resolution performance of the q-GGMRF prior for the image results in Fig. 7. With $p=2.0$, $q=1.2$, and $c=10$, the q-GGMRF presents a good compromise between edge preservation for high contrast and low contrast imaging free of plateauing, compared to either the Gaussian or the GGMRF priors.

Prior	p	q	c	σ	Std. Dev. (HU)	50% MTF (lp/cm)
Gaussian	2.0	2.0	n/a	10	11.15	4.24
q-GGMRF	2.0	1.2	10	8	10.88	7.23
GGMRF	1.1	1.1	n/a	0.1	10.78	8.16

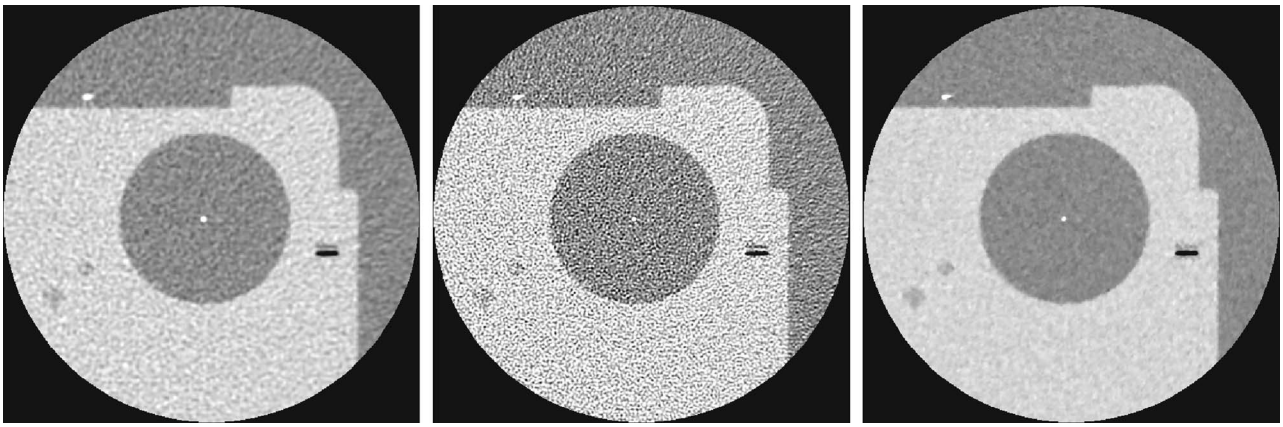

FIG. 8. Comparison of FBP vs MAP-ICD performance on the GE Performance Phantom: 16×0.625 mm, helical pitch 15/16:1, 100 mA, 1 s/rotation, WW=400. Left panel: FBP "standard" kernel. Center panel: FBP "bone" kernel. Right panel: MAP-ICD. MAP-ICD parameters: $\Delta x=\Delta y=0.24$ mm, $\Delta z=0.625$ mm, $p=2.0$, $q=1.2$, $c=10$, $\sigma=16$.

standard deviation of noise of 11.7 HU at 200 mA, while the standard kernel offers a different compromise between image noise and resolution with 50% MTF of 4.3 lp/cm and a 10% MTF of 6.9 lp/cm for a standard deviation of noise of 3.2 HU also at 200 mA. These measurements are for in-plane resolution, and are taken with the GEPP scanned at 1.0 s/rotation and imaged with 2D FBP at 0.625 mm slice thickness.

VII. RESULTS

VII.A. Performance of *q*-GGMRF for in-plane resolution/noise trade-offs

The form of the q-GGMRF prior introduced in Sec. IV depends on three parameters: p and q control the degree of curvature in the potential function in two regions and c determines the boundary between the two. Here we demonstrate the trade-offs in selecting those parameters and arrive at what appears to be a useful compromise.

Iteratively reconstructed CT images will appear different from the FBP images to which radiologists have become accustomed, depending on the parameter choices of the *a priori* image model. These images will gain clinical acceptance only if they avoid characteristics which are disturbing to those reading them. In order to arrive at a sensible choice for the q-GGMRF parameters, we qualitatively compare imagery in Figs. 4–6. The first of these shows several values for p, under the assumption that q assumes an edge-preserving, small value. The choice of $p=2$ shows good edge preservation but also preservation of low contrast information. As the value of p descends from 2, high contrast detail is increasing sharply rendered, but low contrast areas begin to show plateauing and sharp spikes to an objectionable degree. This is due to the strong character of the influence function of the GGMRF with small p near the origin, as shown in Fig. 3. In practice, we prefer the quadratic prior behavior in regions of soft tissue where the presence of lesions may be detected, and the higher resolution of the non-quadratic prior in other regions requiring more detail.

In Fig. 5, we vary the parameter q. It appears that any value for q above 1.4 in this case causes unacceptable levels of smoothing for our attempts at higher resolution reconstructions. At the other extreme, with $p=2.0$ and $q=1.0$, which corresponds to the Huber-Markov model, the degree of salt-and-pepper noise allowed by the strong edge-preserving property becomes objectionable. Again we see that the strongest forms of edge preservation have problematic side effects in other aspects of image quality.

Having evidence that differing exponents in the q-GGMRF for the low and high-contrast regions are desirable, we consider in Fig. 6 the dependence on the threshold between the regions, c, measured in Hounsfield units. Clearly values of 100 and above place large edges into the quadratic penalty range, causing the sort of smoothing witnessed in the Gaussian case earlier. As c approaches zero, the model approaches the GGMRF, with the attendant plateauing found earlier.

Figure 7 and Table I more quantitatively compare three forms of the q-GGMRF. Noise powers are again approximately matched to allow comparison of resolution as measured by the 50% level of the modulation transfer function (MTF). Notice that the GGMRF has the highest spatial resolution, but that the q-GGMRF achieves comparable resolution performance, much greater than with the Gaussian prior. Based on these results, it appears that the values $p=2$, $q=1.2$, and $c=10$ represent a good compromise between resolution, low contrast sensitivity, and high contrast edge preservation at a fixed noise level. Figure 3 also illustrates how

TABLE II. Comparison of FBP and IR for measurement of in-plane MTF and noise, for the images in Fig. 8.

	FBP standard	FBP bone	MAP-ICD
50% MTF (lp/cm)	4.39	8.53	8.66
10% MTF (lp/cm)	7.04	11.90	13.20
Water Std. Dev. (HU)	20.76	85.09	12.76
Plexiglas Std. Dev. (HU)	24.99	90.94	13.01

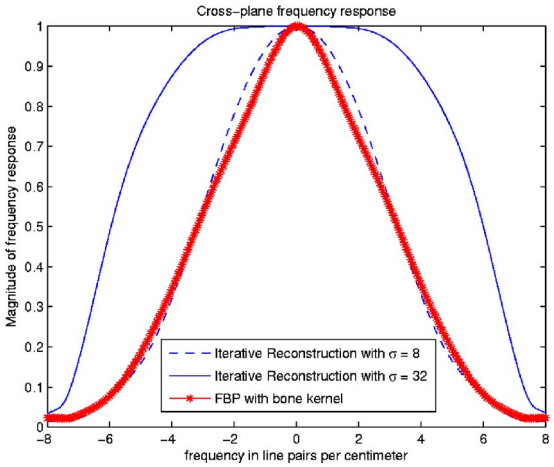

FIG. 9. Cross-plane frequency response comparing FBP to MAP-ICD, corresponding to the images in Fig. 10. For each case, the frequency response is computed by projecting into the sinogram five synthetic points placed in a 10 cm diameter around the isocenter area, and sampling the average of the reconstructed point spread functions in the frequency domain. For MAP-ICD, the calculation is done with a Gaussian prior to matching the analytic model and studying the contrast-independent response. The result shows that MAP-ICD can dramatically improve cross-plane resolution by approaching the theoretical limit more than FBP.

deviations from our preferred selection push the behavior of the prior model toward one of the extreme behaviors of either the Gaussian case or the edge-preserving GGMRF. This choice of parameters achieves visually pleasing image quality. Therefore, we will focus on these prior parameters in our future experiments.

For a comparison at equal resolution between FBP and MAP-ICD reconstruction, we apply the high-frequency "bone" kernel as well as the "standard" kernel in FBP to the wire section of the GEPP. It provides a means to accurately measure the in-plane MTF, while the standard deviation of noise can be measured in the homogeneous regions of the phantom (water and Plexiglas)™. The voxel size is decreased in the reconstructions to properly compute the MTF curves. Results are shown in Fig. 8 and Table II. The measured MTF for the MAP-ICD image is comparable to that of the FBP image reconstructed with the bone kernel, while noise attenuation is close to 50% better in the MAP-ICD image than in the FBP image with the standard kernel.

VII.B. Improvements in cross-plane resolution

Figure 9 shows the frequency response plots resulting from adding synthetic point sources to the head phantom data set with $W=1.25$ mm and a helical pitch of 9/16:1, using the methodology described in Sec. VI. Reconstructions were done with a voxel size of $\Delta_z=0.625$ mm so that the maximum discrete-time frequency of π corresponds to 8 lp/cm. Figure 10 shows the reconstructions associated with each of the three curves. Notice that the frequency response corresponding to MAP-ICD with $\sigma=32$ has much wider MTF than that of FBP, but with comparable levels of noise. In fact, the MAP-ICD can recover frequencies much closer to $1/W$ or 8 lp/cm for this case. On the other hand, the reconstruction with $\sigma=8$ has comparable resolution to FBP, but much lower noise.

The above-noted results are generated with a Gaussian prior to linearly relate the reconstructed images to the data, so that the results are independent of the contrast level. It is possible to achieve even better results with the q-GGMRF and the parameters selected in Sec. VII A thanks to its edge-preserving behavior. In the next results, we apply the q-GGMRF to the three head scans introduced in Sec. VI, comparing results from wide and small detector apertures. Figure 11 compares FDK reconstructions using the bone kernel to the MAP-ICD images. In the MAP-ICD reconstructions, the voxel size is decreased to take advantage of the high sampling rate of the helical scan along the z axis, while conventional analytic approaches cannot easily reduce the slice sensitivity profile without kernel adjustments and enduring a noise penalty. The results demonstrate that the IR images made from the scan with $W=1.25$ mm achieve close to the cross-plane resolution of the FDK images with W

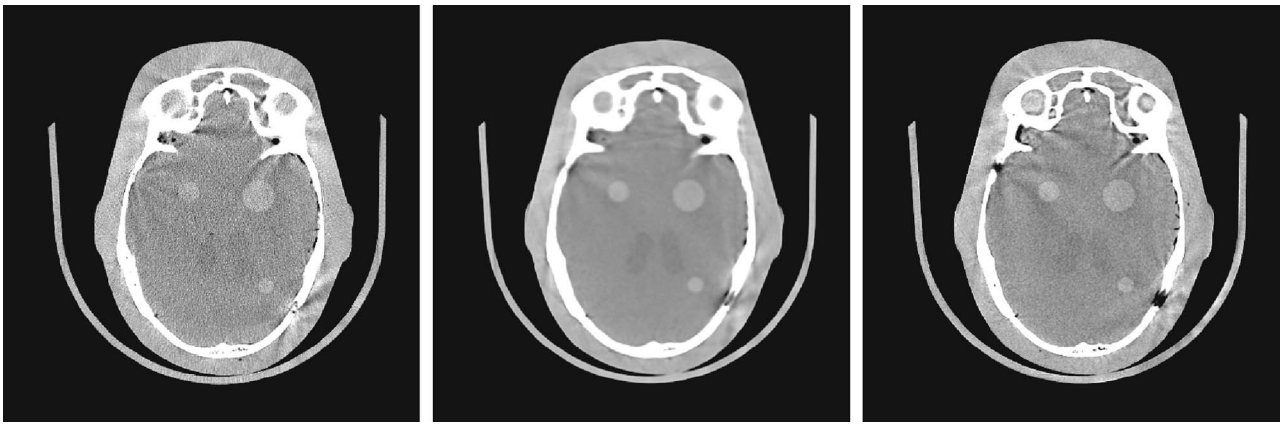

FIG. 10. Head phantom illustrating cross-plane resolution performance and comparing FBP to MAP-ICD, corresponding to the frequency response plots in Fig. 9. The scan is 16×1.25 mm, helical pitch 9/16:1, 100 mA, WW=400. Left panel: 2D FBP "bone" kernel. Center panel: MAP-ICD with $\sigma=8$. Right panel: MAP-ICD with $\sigma=32$. MAP-ICD parameters: $\Delta x=\Delta y=0.244$ mm, $\Delta z=0.625$ mm, $p=2.0$, $q=2.0$, $c=10$. The result shows that MAP-ICD can further improve cross-plane resolution relative to 2D FBP, even with a Gaussian *a priori* model.

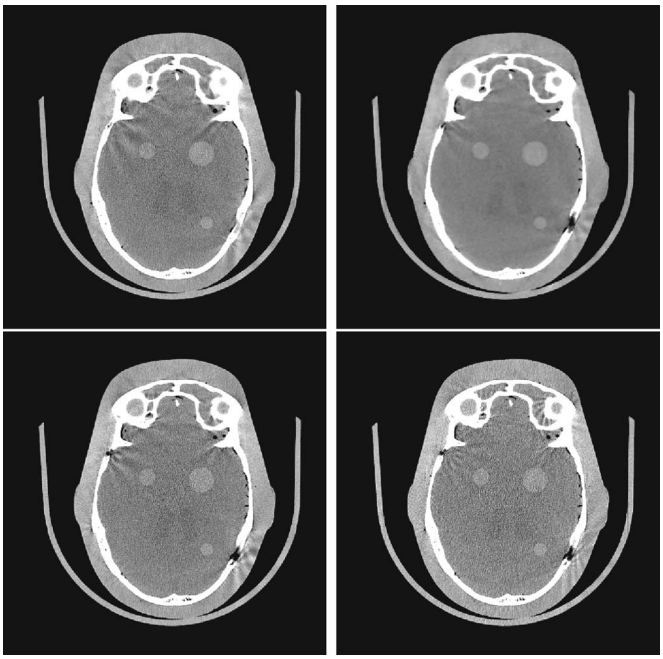

FIG. 11. Qualitative example of improved cross-plane resolution with MAP-ICD. Head phantom, 320 mA, 1 s/rotation, bone kernel, WW=400, $\Delta x=\Delta y=0.488$ mm. Top left panel: 16×1.25 mm pitch 9/16:1 conjugate FDK $\Delta z=1.25$ mm. Top right panel: 16×1.25 mm pitch 9/16:1 MAP-ICD $\Delta z=0.625$ mm, $p=2.0$, $q=1.2$, $c=10$. Bottom left panel: 16×0.625 mm pitch 9/16:1 conjugate FDK $\Delta z=0.625$ mm. Bottom right panel: 16×0.625 mm pitch 15/16:1 FDK $\Delta z=0.625$ mm.

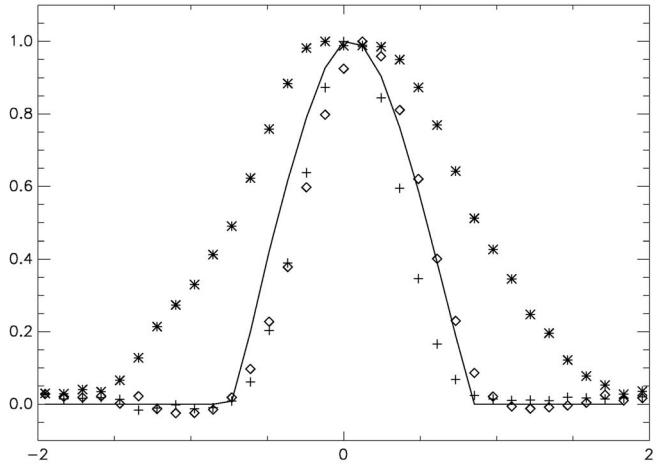

FIG. 13. Normalized slice sensitivity profiles (SSP) plots based on the wire phantom reconstructions in Fig. 14 providing another measure of cross-plane resolution. Horizontal axis represents millimeters; $\Delta x=\Delta y=0.488$ mm. Asterisks: 16×1.25 mm pitch 9/16:1 conjugate FDK $\Delta z=1.25$ mm. Crosses: 16×0.625 mm pitch 9/16:1 conjugate FDK $\Delta z=0.625$ mm. Open triangles: 16×0.625 mm pitch 15/16:1 FDK $\Delta z=0.625$ mm. Solid line: 16×1.25 mm pitch 9/16:1 MAP-ICD $\Delta z=0.625$ mm, $p=2.0$, $q=1.2$, $c=10$.

$=0.625$ mm, while reducing artifacts and image noise at the same time. Details of the fissure in the bone creating an air gap inside the phantom are clearly visible in the MAP-ICD image while even the presence of the gap is not obvious in the FDK image obtained from the same scan. On the other hand, the details of the crack match very well those of FDK reconstructions from the scans with higher sampling, thus validating the MAP-ICD results. These results can also be visualized through multiplanar reformat (MPR) and maximum intensity projection (MIP) renderings of the reconstruction volume focused on the gap in the bone viewed in the sagittal direction, as presented in Fig. 12. Again, the definition of the crack along the z axis with MAP-ICD roughly matches the results from FDK reconstruction of data obtained at twice the sampling rate, while concurrently reducing image noise and artifacts.

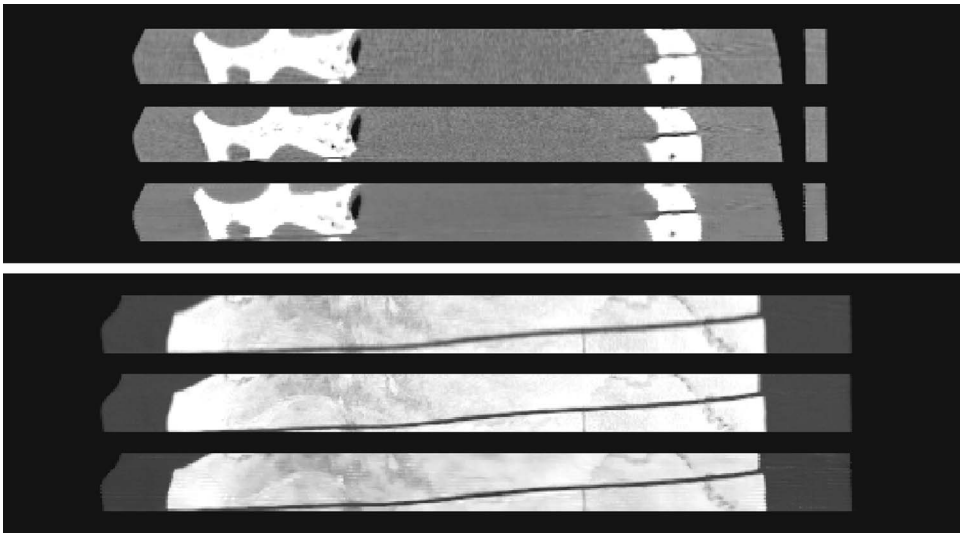

FIG. 12. Qualitative example of improved cross-plane resolution with MAP-ICD (sagittal view). Head phantom. Top panel: Multiplanar reformat (MPR) images. Bottom panel: Maximum intensity projections (MIP) images. With, in each image, from top to bottom: 16×1.25 mm pitch 9/16:1 conjugate FDK; 16×0.625 mm pitch 9/16:1 conjugate FDK; 16×1.25 mm pitch 9/16:1 MAP-ICD. Image spacing is 0.625 mm in the z direction for all images in the reconstructed volume.

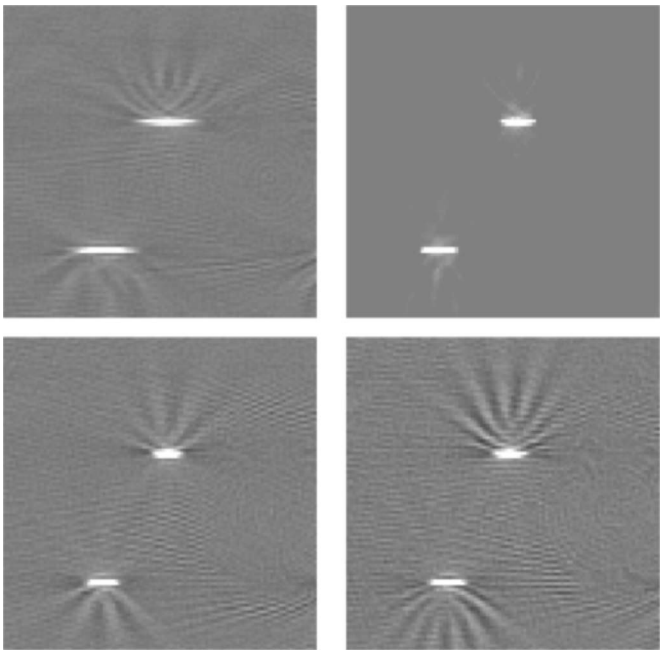

FIG. 14. Wire-in-air phantom used for quantitative measurements of slice sensitivity profile (SSP) based on a 4:1 slope relative to the z axis, with the "bone" kernel, WW=400, $\Delta x=\Delta y=0.488$ mm. Top left panel: 16 $\times$1.25 mm pitch 9/16:1 conjugate FDK $\Delta z=1.25$ mm. Top right panel: 16 $\times$1.25 mm pitch 9/16:1 MAP-ICD $\Delta z=0.625$ mm, $p=2.0$, $q=1.2$, $c=10$, Bottom left panel: 16$\times$0.0625 mm pitch 9/16:1 conjugate FDK Δz =0.625 mm, Bottom right panel: 16$\times$0.625 mm pitch 15/16:1 FDK Δz =0.625 mm.

For quantitative results corroborating the above-noted visual study, SSP measurements obtained from the wire-in-air phantom presented in Sec. VI are shown in Fig. 13 for the same scan protocols as used earlier. Figure 14 shows a zoom over the profile of one of the wires in the axial plane for each of the considered cases. The quantitative measurements taken at 50% and 10% of the maximum SSP intensity (FWHM and FWTM, respectively) shown in Table III confirm the visual results: An improvement of 40% in SSP is achieved with MAP-ICD relative to FDK. Thanks to the edge-preserving behavior of the q-GGMRF model, the SSP curve also falls off to zero more rapidly than in the case of FDK applied to the same scan, and avoids overshoots or undershoots, thus reconstructing clean, well-defined edges.

For a more systematic visual evaluation of z-axis resolution and general image quality, reformats of the AAPM grid phantom referenced in Sec. VI for each of the protocols above appear in Fig. 15. The z direction corresponds to the vertical axis in the reformats. In the MAP-ICD images with $W=1.25$ mm (at the bottom), the smaller 0.4 and 0.5 mm holes on the left-hand side of the phantom are clearly visible, while only the 0.9 mm holes appear clearly separated from FDK-based reconstructions using conjugate backprojection of the same scan (at the top). Interestingly, the 0.6 mm bar pattern (third from the left) is not well resolved in the MAP-ICD reconstruction. This matches very well the prediction based on our model for the frequency response, since 0.6 mm is very close to 0.625 mm, which corresponds to 8 lp/cm, that is the first null in the frequency response for $W=1.25$ mm. Therefore, while the frequencies at the nulls of the frequency response cannot be recovered, the results in Fig. 15 demonstrate resolution recovery beyond the classical resolution of 8 lp/cm with MAP-ICD. The IR technique achieves only slightly lower resolution than that of FDK-based reconstructions with half the detector aperture at W =0.625 mm (middle images from Fig. 15) and higher sampling rate than the above-presented case, consistent with the observations in Fig. 13 and Table III.

TABLE III. SSP measurements at 50% (FWHM) and 10% (FWTM) of the normalized SSP magnitude, obtained from the plots in Fig. 14.

	Algorithm	FWHM (mm)	FWTM (mm)
16$\times$1.25 mm P9/16:1	FDK Conj	1.45	3.12
16$\times$1.25 mm P9/16:1	MAP-ICD	0.89	1.32
16$\times$0.625 mm P9/16:1	FDK Conj	0.63	1.09
16$\times$0.625 mm P15/16:1	FDK Conv	0.72	1.52

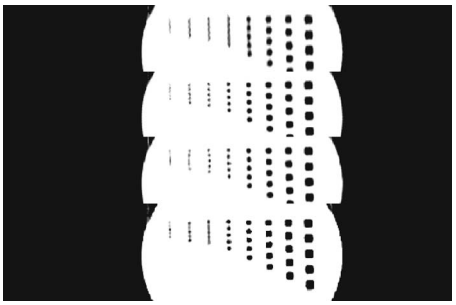

FIG. 15. Visual comparison of cross-plane resolution using reformatted images of the AAPM grid phantom placed upright onto the CT table. FDK uses the "bone" kernel, WW=400, $\Delta x=\Delta y=\Delta z=0.2$ mm. From top to bottom: 16$\times$1.25 mm pitch 9/16:1 conjugate FDK; 16$\times$0.625 mm pitch 9/16:1 conjugate FDK; 16$\times$0.625 mm pitch 15/16:1 FDK; 16$\times$1.25 mm pitch 9/16:1 MAP-ICD, $p=2.0$, $q=1.2$, $c=10$.

VII.C. Reduction of helical artifacts

With the model parameters selected in Sec. VII A and the z-axis resolution performance demonstrated in Sec. VII B, it is important to show that helical artifacts remain under control. In fact, because these artifacts are caused in part by limited sampling rates in the cross-plane direction, the resolution gains discussed in Sec. VII B should help ameliorate them as well.

In Fig. 16, knowledge of the cross section of the head phantom without windmill artifacts is provided in the top left with an axial scan. Significant artifacts remain in the FDK reconstruction, as well as in the Katsevich image. The latter indicates that even though the exact inversion formula treats the exact 3D geometry of data acquisition with a high degree of accuracy, limited sampling dominates image quality. In this case, MAP-ICD can once again take advantage of smaller image voxels and improved resolution to significantly reduce the artifact. This result is further confirmed with reconstructions of the rib phantom in Fig. 17. In the

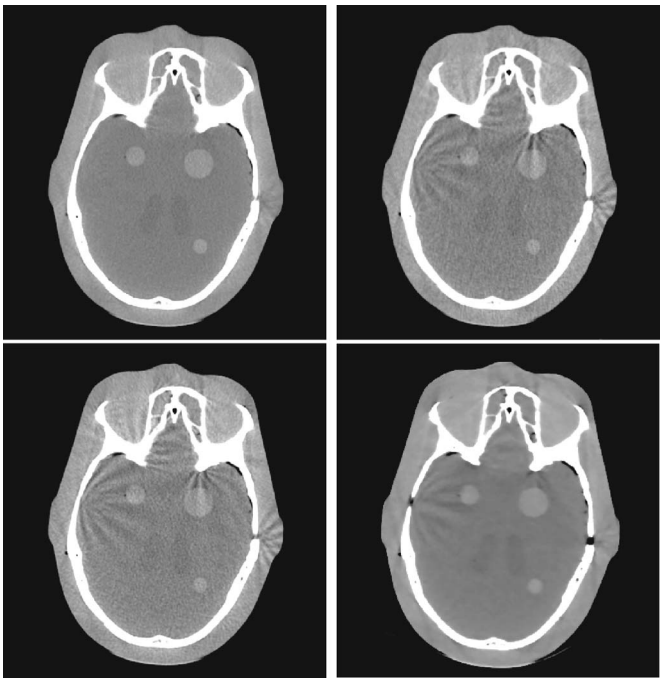

FIG. 16. Comparison of various analytical reconstruction algorithms and MAP-ICD relative to helical artifacts due to limited sampling on a head phantom, 16×1.25 mm, helical pitch 15/16:1, 320 mA, 1 s/rotation, WW =400. Top left panel: Reference axial FBP. Bottom left panel: Feldkamp-based. Top right panel: Katsevich-based; and bottom right panel: MAP-ICD. MAP-ICD parameters: $\Delta x=\Delta y=0.488$ mm, $\Delta z=0.625$ mm, $p=2.0$, $q=1.2$, $c=10$. MAP-ICD can reduce helical artifacts as well or better than approximate or even exact analytical inversion approaches.

FBP image, blurring of the ribs as well as adjacent shading are apparent due to the orientation of the ribs in three dimensions and the high helical pitch of the scan, which reduces sampling coverage. Windmill artifacts also surround the tapered hole. MAP-ICD removes nearly all these artifacts.

VII.D. Clinical results

Finally, the results of this study would not hold without successful application to real clinical data. For this, we reconstruct a human head scan, in order to observe both brain

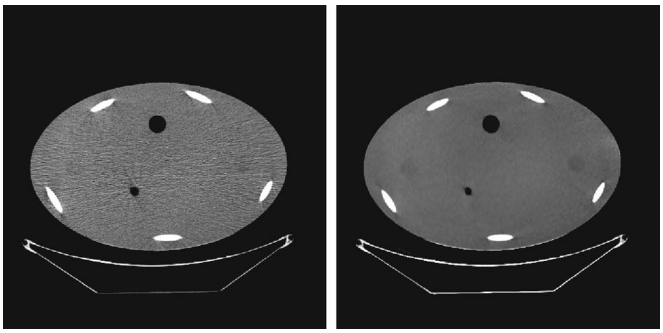

FIG. 17. Illustration of the reduction in helical artifacts for MAP-ICD (right) vs 2D FBP (left) on a Rib Phantom scanned in 8×1.25 mm helical mode, pitch 13.4/8:1, 320 mA, 0.5 s/rotation, WW=400. FBP parameters: $\Delta x=\Delta y=0.488$ mm, $\Delta z=1.25$ mm, "standard" kernel; MAP-ICD parameters: $\Delta x=\Delta y=0.488$ mm, $\Delta z=0.625$ mm, $p=2.0$, $q=1.2$, $c=10$.

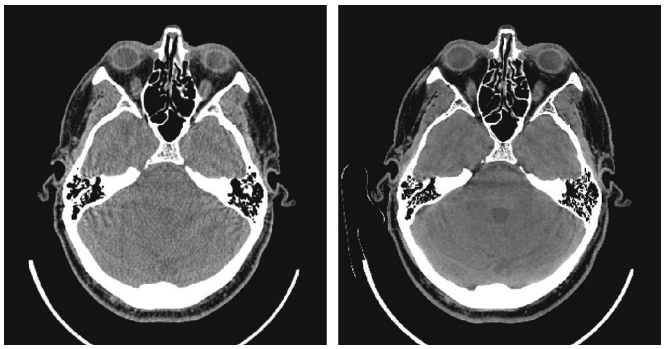

FIG. 18. Qualitative clinical results on a human head: standard FBP (left) vs MAP-ICD (right) 32×0.625 mm helical scan, pitch 17/32:1, 140 kV, 280 mA, WW=300. Reconstruction parameters: $\Delta x=\Delta y=0.586$ mm, $\Delta z=1.2$ mm, $p=2.0$, $q=1.2$, $c=10$. The MAP-ICD image is not fully corrected for beam hardening artifacts.

soft tissue and bone. Figure 18 confirms that on clinical data as well, MAP-ICD demonstrates significantly improved image quality, most dramatically achieved by reducing the level of noise. Small vessels and other structures present in the fat and soft tissue around the skull or near the orbits appear clearly in the IR image while they remain mostly hidden by noise in the FBP image. The improvement in resolution is particularly visible around the sinus area, where the thin walls between the sinus cavities are more clearly visible in the IR image, and in the detail of the air cells in the inner ear region. The reduction of noise in the posterior fossa and the temporal lobes allows better examination of the brain tissue, improving the low contrast differentiation between the cerebellum and the fourth ventricle, visible as a darker region in the center of the posterior fossa. Meanwhile, the helical artifacts that distort the brain tissue near the inner ear in the FBP image are quite satisfactorily removed from the MAP-ICD image. We note that beam hardening artifacts are still present in the brain stem region as well as at the base of the skull, which is not surprising since our model does not explicitly account for beam hardening beyond a simple precorrection at this time. Nonetheless, one could argue that the novel texture of the image, although significantly different from conventional FBP, may provide better diagnostic value overall.

VIII. DISCUSSION

The general results presented earlier illustrate several major aspects of our iterative algorithm. First, good balance between carefully designed statistical noise and image regularization models needs to be achieved to provide an acceptable solution to the CT reconstruction problem. The q-GGMRF analytical prior we introduced in this paper provides necessary flexibility in its parameters to control the behavior both around the origin and at the tails of the distribution, and appears better suited to clinical CT imaging than the conventional Gaussian or GGMRF priors. Its parametrization through p, q, and c is understood well enough to produce promising preliminary results. The last remaining parameter is σ, which controls the prior strength over the noise model, and currently remains empirically adjusted for best

image quality, when the prior strength is sufficient to control noise without leading to oversmoothing. A more systematic way of setting σ is needed. A consequence of the constant nature of this parameter on the reconstruction may be nonuniform resolution as the trade-off between varying confidence weighting in ray projections and nonlinear image smoothing is not actively managed. With constant σ, the result of a spatially variant noise model is also spatially variant resolution,[56] which can lead to directional blurring of edges. Fessler recently proposed a framework to help with this issue in the quadratic case,[57] relying on the global interaction among image model, noise model, and system forward model.

Another major differentiating aspect of IR relative to conventional analytical algorithms is precisely the quality of the description of the interaction between image and detector elements. Detector and voxel responses are explicitly included in the forward model. Nearly all analytical reconstruction techniques assume the presence of continuous sampling. In the discrete implementation, therefore, either projection domain or image domain interpolations have to be performed. Because the interpolation techniques often fail to preserve high-frequency contents, a loss of spatial resolution in the reconstructed images often results. In a FDK-type reconstruction algorithm with linear interpolation, for example, it has been shown that nearly 30% reduction in z resolution may occur.[58] Higher order interpolations incur a significant penalty in image noise.[59] In other cases, to reduce aliasing artifacts, z-smoothing algorithms are often employed and further reduce the spatial resolution in z. By contrast, the geometric model used in statistical methods is intrinsically spatially variant and makes better use of the sinogram information. While analytical methods must use advanced techniques such as focal spot wobble[60] or conjugate-ray backprojection[52] to achieve greater resolution, IR methods may already recover frequencies closer to the maximum system resolution without this extra information. In the view of iterative reconstruction, conjugate samples do not provide additional information, contrary to the case of analytical backprojection, where they can help reduce interpolation errors due to discrete detector sampling. In addition, forward modeling may also include such second-order effects as focal spot size, physical detector response, and nonidealities in scanning trajectory introduced by the CT tube or table, all of which may result in better resolution.

The above-presented results emphasize cross-plane resolution in the multislice helical geometry. Because of the continuous motion of the CT table and high DAS trigger frequencies, helical scanning implies a very high sampling rate in the z dimension. A quick calculation of the total number of available samples relative to the number of unknown image elements under a simplified view of the linear problem as $\mathbf{y} \approx \mathbf{A}\mathbf{x}$ may show easily that reconstruction does not suffer from underdetermination. In fact, to recover frequencies less than $1/W$ that corresponds to the first null of the sine function we discussed in Sec. VI, Nyquist dictates that the sampling frequency should be $2/W$, which is sample period $W/2$. Therefore, IR techniques should theoretically reconstruct images at half the detector width to recover the highest frequency. This is consistent with all the reconstruction experiments in Sec. VII where MAP-ICD typically uses $\Delta_z = 0.625$ mm for $W = 1.25$ mm. With these parameters, it appears that we may even be able to recover frequencies that lie beyond the first null in the frequency response, as illustrated in Fig. 15.

Finally, we cannot compare iterative reconstruction to analytical methods without commenting on computation speed. High model accuracy leads to complexity in the calculations, and multiple passes over the data are needed to reach convergence. For a 16-slice high resolution case such as those considered in Sec. VII, current serial implementation still requires in excess of 12 h for reconstruction of the portion of the volume covered by the scanning trajectory over a handful of gantry rotations. We have proposed some acceleration methods for the algorithm, for instance, improving the order of the ICD updates,[61] or replacing the half-interval search with a one-step approach.[62] But overall reconstruction time remains a significant challenge, short of possible hardware optimization.

IX. CONCLUSION

We have presented a Bayesian framework for iterative CT image reconstruction that produces significant improvements over direct analytical methods in terms of noise, resolution, and helical artifacts. As the reconstruction technique remains independent from the exact form of the forward model, this method is applicable to any geometry and is particularly well suited to the multislice helical problem. We introduced a novel model for image statistics providing further control over image quality for clinical application. We also presented an analysis of cross-plane resolution performance to support the superior results of our iterative algorithm relative to conventional analytical reconstruction. Computational speed remains a particular challenge for the practical application of IR methods with high accuracy in clinical CT, because spatially varying geometric models do not easily lend themselves to the kind of hardware optimizations which have allowed reconstruction performance of multiple frames per second for analytical algorithms on current commercial scanners. In addition, the nonlinear problem formulation generates novel image appearance which may be disturbing at first for clinicians who are accustomed to the well-understood properties of linear reconstruction techniques. Ultimately, the success of IR methods in clinical applications will depend on the demonstration of potential improvement in diagnostic readability, or modified scanning protocols to the benefit of the patient.

APPENDIX: PROOF OF CONVEXITY OF PRIOR MODEL

This appendix presents the analytic proof of convexity of the q-GGMRF prior regularization term, thus guaranteeing global convergence properties of the ICD algorithm over the MAP functional in Eq. (4). The potential function of the q-GGMRF has been defined in Sec. IV, and takes the form:

$$\rho(\Delta)=\frac{|\Delta|^p}{1+|\Delta/c|^{p-q}}.$$

In this paragraph, we demonstrate the convexity of this prior function under the following assumption: the q-GGMRF function defined in Eq. (16) is convex for $1\leqslant q\leqslant p\leqslant 2$.

First, define $r=p-q$. If $1\leqslant q\leqslant p\leqslant 2$, then we know that $1\leqslant p\leqslant 2$ and $0\leqslant r\leqslant p-1$. If $r=0$ and $p\geqslant 1$, then $\rho(\Delta)$ defaults to the GGMRF, and the function is clearly convex. Without loss of generality for this analysis, consider also $c=1$. Then, define the function:

$$g(x,p,r)=\frac{|x|^p}{1+|x|^r}.$$

The first derivative of $\rho(\Delta)$ has been calculated in Eq. (17). Noticing that the equation can be factorized and rewritten as a function of $g(\cdot)$, we obtain for the first derivative of g:

$$g'(x,p,r)=g(x,p-1,r)[p-rg(x,r,r)]\text{sign}(x).$$

The second derivative is then given by

$$\begin{aligned}g''(x,p,r)&=g'(x,p-1,r)[p-rg(x,r,r)]\text{sign}(x)-rg(x,p-1,r)g'(x,r,r)\text{sign}(x)\\&=g(x,p-2,r)[p-1-rg(x,r,r)][p-rg(x,r,r)]-rg(x,p-1,r)g(x,r-1,r)[r-rg(x,r,r)]\\&=g(x,p-2,r)[p-1-rg(x,r,r)][p-rg(x,r,r)]-r^2g(x,p-1,r)g(x,r-1,r)[1-g(x,r,r)].\end{aligned}$$

Note that

$$g(x,p,r)=|x|^{p-r}g(x,r,r),$$

$$g(x,r,r)=|x|g(x,r-1,r).$$

So

$$\begin{aligned}g''(x,p,r)&=|x|^{p-r-2}g(x,r,r)[p-1-rg(x,r,r)]\times[p-rg(x,r,r)]-r^2|x|^{p-r-1}g(x,r,r)\\&\quad\times\frac{1}{|x|}g(x,r,r)[1-g(x,r,r)]\\&=r^2|x|^{p-r-2}g(x,r,r)\times\left[\left(\frac{p-1}{r}-g(x,r,r)\right)\left(\frac{p}{r}-g(x,r,r)\right)-g(x,r,r)(1-g(x,r,r))\right].\end{aligned}$$

The function $g(x,p,r)$ is convex if and only if $g''(x,p,r)\geqslant 0$, which therefore translates to

$$\left(\frac{p-1}{r}-g(x,r,r)\right)\left(\frac{p}{r}-g(x,r,r)\right)-g(x,r,r)(1-g(x,r,r))\geqslant 0.$$

This is true if and only if for all x, we have

$$\frac{((p-1)/r-g(x,r,r))(p/r-g(x,r,r))}{g(x,r,r)(1-g(x,r,r))}\geqslant 1. \tag{A1}$$

Some properties of $g(x,r,r)$ are

(1) $g(0,r,r)=0$
(2) $\lim_{x\to\infty}g(x,r,r)=1$
(3) $\forall x\geqslant 0$, $g(x,r,r)$ is a monotonically increasing function of x
(4) $\{g(x,r,r):x\in\mathbb{R}\}=[0,1)$

Using property 4 and criterion (A1), we have the necessary and sufficient criterion that for all $\rho\in[0,1)$

$$\frac{((p-1)/r-\rho)(p/r-\rho)}{\rho(1-\rho)}\geqslant 1. \tag{A2}$$

Remember that $1\leqslant p\leqslant 2$ and $0\leqslant r\leqslant p-1$. Using this constraint, we have that

$$\frac{p-1}{r}\geqslant\frac{p-1}{p-1}=1.$$

Similarly, we have that

$$\frac{p}{r}\geqslant\frac{p}{p-1}\geqslant 2.$$

So therefore

$$\frac{((p-1)/r-\rho)(p/r-\rho)}{\rho(1-\rho)}\geqslant\frac{(2-\rho)(1-\rho)}{\rho(1-\rho)}=\frac{2-\rho}{\rho}\geqslant 1. \tag{A3}$$

This concludes the proof that the q-GGMRF is convex for $1\leqslant q\leqslant p\leqslant 2$.

[a]Electronic mail: jean-baptiste.thibault@med.ge.com
[b]Electronic mail: sauer@nd.edu
[c]Electronic mail: bouman@purdue.edu
[d]Electronic mail: jiang.hsieh@med.ge.com

[1]K. Sourbelle and W. Kalender, "Generalization of Feldkamp reconstruction for clinical spiral cone beam CT," in Proceeding of the International Conference on Fully 3D Reconstruction in Radiology and Nuclear Medicine, Saint Malo, France, 29 June–4 July 2003.
[2]X. Tang, J. Hsieh, R. Nilsen, S. Dutta, D. Samsonov, and H. Hagiwara, "A three-dimensional weighted cone beam filtered backprojection (CB-FBP) algorithm for image reconstruction in volumetric CT - helical scanning," Phys. Med. Biol. **51**, 855–874 (2006).
[3]M. Silver and K. Taguchi, "Windmill artifacts in multislice helical CT," in Proceedings of SPIE Conference on Medical Imaging, Vol. 5032, May 2003, pp. 1918–1927.
[4]K. Taguchi and H. Aradate, "Algorithm for image reconstruction in multislice helical CT," Med. Phys. **25**, 550–561 (1998).
[5]H. Hu, "Multi-slice helical CT: Scan and reconstruction," Med. Phys. **26**, 1–18 (1999).
[6]J. Hsieh, "A generalized helical reconstruction algorithm for multi-slice CT," Radiology **217**, 565 (2000).
[7]D. Heuscher, "Helical cone beam scans using oblique 2d surface reconstructions," in *Proceedings of the International Conference on Fully 3D Reconstruction in Radiology and Nuclear Medicine*, Egmond aan Zee, The Netherlands, 23–26 June 1999, pp. 204–207.
[8]H. Turbell and P.-E. Danielsson, "An improved PI-method for reconstruction from helical cone beam projections," in *Conference Record of the IEEE Medical Imaging Conference*, Vol. 2, Seattle, WA, 24–30 October 1999, pp. 865–868.
[9]R. Proksa, T. Koehler, M. Grass, and J. Timmer, "The *n*-PI method for helical cone-beam CT," IEEE Trans. Med. Imaging **9**, 848–863 (2000).

[10]M. Kachelrieß, S. Schaller, and W. Kalender, "Advanced single-slice rebinning in cone-beam spiral CT," Med. Phys. **4**, 754–772 (2000).
[11]T. Flohr, K. Stierstorfer, H. Bruder, J. Simon, A. Polacin, and S. Schaller, "Image reconstruction and image quality evaluation for a 16-slice CT scanner," Med. Phys. **5**, 832–845 (2003).
[12]L. Feldkamp, L. Davis, and J. Kress, "Practical cone-beam algorithm," J. Opt. Soc. Am. A **1**, 612–619 (1984).
[13]X. Tang and J. Hsieh, "A helical cone beam filtered backprojection (CB-FBP) reconstruction algorithm using three-dimensional (3D) view-weighting," Proc. SPIE **5535**, 577–587 (2004).
[14]I. Hein, K. Taguchi, M. Silver, M. Kazarna, and I. Mori, "Feldkamp-based cone-beam reconstruction for gantry-tilted helical multislice CT," Med. Phys. **12**, 3233–3242 (2003).
[15]K. Stierstorfer, A. Rauscher, J. Boese, H. Bruder, S. Schaller, and T. Flohr, "Weighted fbp - A simple approximative 3d fbp algorithm for multislice spiral ct with good dose usage for arbitrary pitch," Phys. Med. Biol. **49**, 2209–2218 (2004).
[16]A. Katsevich, "Analysis of an exact inversion algorithm for spiral cone-beam CT," Phys. Med. Biol. **47**, 2583–2597 (2002).
[17]F. Noo, J. Pack, and D. Heuscher, "Exact helical reconstruction using native cone-beam geometries," Phys. Med. Biol. **48**, 3787–3818 (2003).
[18]J.-B. Thibault, K. Sauer, C. Bouman, and J. Hsieh, "High quality iterative image reconstruction for multi-slice helical CT," in *Proceedings of the International Conference on Fully 3D Reconstruction in Radiology and Nuclear Medicine*, Saint Malo, France, 29 June–4 July 2003.
[19]J.-B. Thibault, K. Sauer, C. Bouman, and J. Hsieh, "Three-dimensional statistical modeling for image quality improvements in multi-slice helical CT," in *Proceedings of the International Conference on Fully 3D Reconstruction in Radiology and Nuclear Medicine*, Salt Lake City, UT, 6–9 July 2005, pp. 271–274.
[20]D. Politte, S. Yan, J. O'Sullivan, D. Snyder, and B. Whiting. "Implementation of alternating minimization algorithms for fully 3D CT imaging," in *Proceedings of the SPIE/IS&T Symposium on Electronic Imaging Science and Technology—Computational Imaging* Vol. 5674, San Diego, CA,2005.
[21]A. Ziegler, T. Koehler, T. Nielsen, and R. Proksa, "Iterative cone-beam CT image reconstruction with spherically symmetric basis functions," in *Proceeding of the International Conference on Fully 3D Reconstruction in Radiology and Nuclear Medicine*, Salt Lake City, UT, 6–9 July 2005, pp. 80–83.
[22]M. Knaup, W. Kalender, and M. Kachelrieß, "Statistical cone-beam CT image reconstruction using the cell broadband engine," in *Conference Record of the 2006 Medical Imaging Conference*, San Diego, CA, 29 October–November 2006.
[23]F. Beekman and C. Kamphuis, "Ordered subset reconstruction for x-ray CT," Phys. Med. Biol. **46**, 1835–1844 (2001).
[24]J. Fessler, "Hybrid Poisson/polynomial objective functions for tomographic image reconstruction from transmission scans," IEEE Trans. Image Process. **4**, 1439–1450 (1995).
[25]K. Lange and J. Fessler, "Globally convergent algorithms for maximum *a posteriori* transmission tomography," IEEE Trans. Image Process. **4**, 1430–1450 (1995).
[26]J. Nuyts, B. D. Man, P. Dupon, M. Defrise, P. Suetens, and L. Mortelmans, "Iterative reconstruction for helical CT: A simulation study," Phys. Med. Biol. **43**, 729–737 (1998).
[27]J. Hsieh, *Computed Tomography: Principles, Design, Artifacts, and Recent Advances* (SPIE, Bellingham, WA, 2003).
[28]C. Bouman and K. Sauer, "A unified approach to statistical tomography using coordinate descent optimization," IEEE Trans. Image Process. **5**, 480–492 (1996).
[29]K. Sauer and C. Bouman, "A local update strategy for iterative reconstruction from projections," IEEE Trans. Image Process. **41**, 534–548 (1993).
[30]J.-B. Thibault, C. Bouman, K. Sauer, and J. Hsieh, "A recursive filter for noise reduction in statistical iterative tomographic imaging," in *Proceeding of the SPIE/IS&T Symposium on Electronic Imaging Science and Technology—Computational Imaging*, Vol. 6065, San Jose, CA, 15–19 January 2006.
[31]B. Whiting and P. Massoumzadeh, "Properties of preprocessed sinogram data in x-ray computed tomography," Med. Phys. **33**, 3290–3303 (2006).
[32]E. Ü. Mumcuoğlu, R. Leahy, S. Cherry, and Z. Zhou, "Fast gradient-based methods for Bayesian reconstruction of transmission and emission pet images," IEEE Trans. Med. Imaging **13**, 687–701 (1994).
[33]H. Erdogan and J. Fessler, "Ordered subsets algorithms for transmission tomography," Phys. Med. Biol. **44**, 2835–2851 (1999).
[34]R. Siddon, "Fast calculation of the exact radiological path for a three-dimensional CT array," Med. Phys. **12**, 252–255 (1985).
[35]F. Jacobs, E. Sundermann, B. D. Sutter, M. Christiaens, and I. Lemahieu, "A fast algorithm to calculate the exact radiological path through a pixel or voxel space," J. Comput. Info. Technol. **6**, 89–94 (1998).
[36]B. DeMan and S. Basu, "Distance-driven projection and backprojection in three-dimensions," Phys. Med. Biol. **49**, 2463–2475 (2004).
[37]D. Young, *Iterative Solution of Large Linear Systems* (Academic, New York, 1971).
[38]D. Rogers, *Procedural Elements for Computer Graphics*, 2nd ed. (McGraw-Hill, Boston, 1998).
[39]S. Geman and D. McClure, "Statistical methods for tomographic image reconstruction," Bull. Internat. Statist. Inst. **LII-4** 5–21 (1987).
[40]L. Shepp and Y. Vardi, "Maximum likelihood reconstruction for emission tomography," IEEE Trans. Med. Imaging **MI-1**, 113–122 (1982).
[41]C. Bouman and K. Sauer, "A generalized Gaussian image model for edge-preserving MAP estimation," IEEE Trans. Image Process. **2**, 296–310 (1993).
[42]A. Blake and A. Zisserman, *Visual Reconstruction* (MIT, Cambridge, 1987).
[43]J. Besag, "Towards Bayesian image analysis," J. Appl. Stat. **16**, 395–407 (1989).
[44]P. Green, "Bayesian reconstruction from emission tomography data using a modified EM algorithm," IEEE Trans. Med. Imaging **9**, 84–93 (1990).
[45]R. Stevenson and E. Delp, "Fitting curves with discontinuities," *Proceedings of the First International Workshop on Robust Computer Vision*, Seattle, WA, 1–3 October 1990, pp. 127–136.
[46]D. Geman and G. Reynolds, "Constrained restoration and the recovery of discontinuities," IEEE Trans. Pattern Anal. Mach. Intell. **14** 367–383 (1992).
[47]S. Brette, J. Idier, and A. Mohammad-Djafari, "Scale invariant Markov models for Bayesian inversion linear inverse problems," in *Maximum Entropy and Bayesian Methods*, edited by J. Skilling and S. Sibisi (Kluwer Academic, Dordrecht, 1996), pp. 199–212.
[48]V. Panin, G. Zeng, and G. Gullberg, "Total variation regulated EM algorithm," IEEE Trans. Nucl. Sci. **46**, 2202–2210 (1999).
[49]B. D. Man, S. Basu, J.-B. Thibault, J. Hsieh, J. Fessler, K. Sauer, and C. Bouman, "A study of different minimization approaches for iterative reconstruction in x-ray CT," in *Proceedings of the IEEE Nuclear Science Symposium and Medical Imaging Conference*, Vol. 3, San Juan, Puerto Rico, 23–29 October 2005, pp. 2708–2710.
[50]J.-B. Thibault, K. Sauer, and C. Bouman, "Newton-style optimization for emission tomographic estimation," J. Electron. Imaging **9**, 269–282 (2000).
[51]J. Zheng, S. Saquib, K. Sauer, and C. Bouman, "Parallelizable Bayesian tomography algorithms with rapid, guaranteed convergence," IEEE Trans. Image Process. **9**, 1745–1759 (2000).
[52]J. Hsieh, X. Tang, J.-B. Thibault C. Shaughnessy, and R. Nilsen, "Conjugate cone beam backprojection for high z-resolution reconstruction," in *Proceedings of the International Conference on Fully 3D Reconstruction in Radiology and Nuclear Medicine*, Salt Lake City, UT, 6–9 July 2005, pp. 137–141.
[53]E. DuBois, "The sampling and reconstruction of time-varying imagery with application in video systems," Proc. IEEE **73**, 502–522 (1985).
[54]D. Early and D. Long, "Image reconstruction and enhanced resolution imaging from irregular samples," IEEE Trans. Geosci. Remote Sens. **39**, 291–302 (2001).
[55]"Phantoms for performance evaluation and quality assurance of CT scanners," AAPM Task Force on CT Scanner Phantoms, American Association of Physicists in Medicine, Tech. Rep. ISBN 1-888340-04-5, 1977.
[56]J. Fessler and W. Rogers, "Spatial resolution properties of penalized-likelihood image reconstruction methods: Space-invariant tomographs," IEEE Trans. Image Process. **5**, 1346–1358 (1996).
[57]J. Fessler, "Analytical approach to regularization design for isotropic spatial resolution," in *IEEE Nuclear Science Symposium & Medical Imaging*, Vol. 3, Portland, OR, 19–25 October 2003, pp. 2022–2026.
[58]J. Hsieh, "Analytical model for multi-slice helical CT performance parameters," Med. Phys. **30**, 169–178 (2003).
[59]J. Hsieh, "Investigation of an image artifact induced by projection noise inhomogeneity in multi-slice helical computed tomography," Phys. Med. Biol. **48**, 341–356 (2003).

[60]K. Stierstorfer and T. Flohr, "A reconstruction procedure for CT systems with z-sharp technology," in *Proceedings of the International Conference on Fully 3D Reconstruction in Radiology and Nuclear Medicine*, Salt Lake City, UT, 6–9 July 2005, pp. 28–30.
[61]Z. Yu, J.-B. Thibault, C. Bouman K. Sauer, and J. Hsieh, "Non-homogeneous updates for the iterative coordinate descent algorithm," in *Proceedings of the SPIE/IS&T Symposium on Electronic Imaging Science and Technology—Computational Imaging*, Vol. 6498, San Jose, CA, 29–31 January 2007.
[62]Z. Yu, J.-B. Thibault, K. Sauer, C. Bouman, and J. Hsieh, "Accelerated line search for coordinate descent optimization," in *Proceedings of the IEEE Nuclear Science Symposium and Medical Imaging Conference*, Vol. 6498, San Jose, 29 October–4 November 2006, pp. 2841–2844.

Errata for:

J.-B. Thibault, K. Sauer, C. Bouman, and J. Hsieh, "A Three-Dimensional Statistical Approach to Improved Image Quality for Multi-Slice Helical CT," *Medical Physics,* pp. 4526-4544, vol. 34, no. 11, November 2007.

Authored: Pengchong Jin (jin36@purdue.edu) and Charles A. Bouman (bouman@purdue.edu)
Updated: May 10, 2013

- Equation (5): The correct equation should be

$$\tilde{\theta} = \left(\theta + \frac{\pi}{4}\right) mod \ \frac{\pi}{2} - \frac{\pi}{4}$$

- Figure 2: The coordinate system in the right figure is **radial** and z, not y and z.

- Equation (10): The correct equation should be

$$S(\delta) = \frac{1}{D} rect\left(\frac{\delta}{D}\right)$$

- Equation (11): The correct equation should be

$$A_{i,j,k} = \frac{\Delta_{xy}}{D_c \cos\tilde{\theta}} \ clip\left[0, \frac{D_c + L_c}{2} - |\delta_c|, \min(L_c, D_c)\right]$$

- Equation (12): The correct equation should be

$$B_{i,j,k,l} = \frac{1}{D_r \cos\varphi} \ clip\left[0, \frac{D_r + L_r}{2} - |\delta_r|, \min(L_r, D_r)\right]$$